NASA Technical Paper 1224

Static Performance of Five Twin-Engine Nonaxisymmetric Nozzles With Vectoring and Reversing Capability

Francis J. Capone

JULY 1978

NASA Technical Paper 1224

Static Performance of Five Twin-Engine Nonaxisymmetric Nozzles With Vectoring and Reversing Capability

Francis J. Capone
Langley Research Center
Hampton, Virginia

National Aeronautics
and Space Administration

**Scientific and Technical
Information Office**

1978

SUMMARY

An investigation has been conducted in the static-test facility of the Langley 16-foot transonic tunnel to determine the static performance of five twin-engine nonaxisymmetric nozzles and a base-line axisymmetric nozzle at three nozzle power settings. Static thrust-vectoring and thrust-reversing performance were also determined. Nonaxisymmetric-nozzle concepts included two-dimensional convergent-divergent nozzles, wedge nozzles, and a nozzle with a single external-expansion ramp. Thrust vectoring for the various concepts was accomplished by subsonic turning, supersonic shock deflection, supersonic expansion turning, or some combination of these, depending on the nozzle concept.

The two-dimensional convergent-divergent nozzles had essentially the same performance as the base-line axisymmetric nozzle. For the dry- or cruise-power setting at the nozzle design pressure ratio of 3.5, the nozzles with external-expansion surfaces had a lower performance than the axisymmetric nozzle by 2.0 to 2.3 percent. Thrust-vectoring performance was highly dependent upon the type of flow turning employed. Those nozzles that used only subsonic turning had essentially no thrust losses due to thrust vectoring up to 30° deflection. The nozzle with supersonic shock deflection (a single-expansion ramp-type nozzle) had the lowest performance with losses as high as 7.5 percent. One two-dimensional convergent-divergent nozzle achieved a reverse-thrust level of 50 percent of the forward thrust. Two other configurations had reverse-thrust levels of 10 to 25 percent of the forward thrust. However, these two nozzle configurations may have greater reverse-thrust levels by the use of full sideplates.

INTRODUCTION

Recent studies on twin-engine fighter airplanes (refs. 1 to 5) have identified potential benefits for nonaxisymmetric nozzles in the areas of improved integration for installed drag reduction, thrust vectoring for maneuver enhancement and short field take-off and landing, and thrust reversing for improved agility and ground handling. Experimental studies (refs. 6 to 8) have identified drag-reduction payoffs for nonaxisymmetric wedge nozzles, especially for twin-engine configurations (ref. 8). Thrust vectoring has been shown to offer increased configuration lift (refs. 2 and 9), and significant in-flight thrust-reversal levels have been demonstrated for a nonaxisymmetric wedge nozzle (ref. 8). A detailed nozzle-engine integration study that included a comprehensive series of aerodynamic and mechanical design studies, scale model test programs, and a full-scale nozzle-engine static test has recently been conducted (refs. 5 and 10) on a single external-expansion ramp-type nozzle. However, the true potential of nonaxisymmetric nozzles will be realized only if performance levels and weights comparable to conventional axisymmetric levels are achieved.

A number of promising nonaxisymmetric-nozzle concepts were identified in the study of reference 3. The Langley Research Center is cooperating in a follow-on program being conducted by the McDonnell Douglas Corporation for the U.S. Air Force Flight Dynamics Laboratory. The objectives of this program are to determine experimentally the internal and installed performance levels of several nonaxisymmetric-nozzle concepts and to quantify nozzle-airframe interactive effects for use in the development of aircraft configurations which take advantage of the benefits of these nozzle types. Further details including a discussion of the various nozzles are given in reference 11.

This paper presents the internal performance of five different nonaxisymmetric nozzles plus a base-line axisymmetric nozzle at static conditions. Performance at vectored and reverse-thrust conditions are also presented. Summaries of these results were presented in reference 11. This investigation was conducted in the static-test facility of the Langley 16-foot transonic tunnel.

SYMBOLS

All forces and angles are referred to the model center line (fig. 1). A discussion of the data-reduction procedure and definitions of forces, angles, and propulsion relationships used herein are given in the appendix.

A_e nozzle-exit area, cm^2

A_{max} model maximum cross-sectional area, 284.78 cm^2

A_t nozzle-throat area, cm^2

$C_{F,i}$ ideal isentropic gross thrust coefficient, $F_i/p_a A_{max}$

d_e nozzle-exit height, cm

d_n nozzle height at leading edge of convergent flap for 2-D C-D/1 nozzle, cm (fig. 9)

d_t nozzle-throat height, cm

$F_{A,bal}$ resultant axial force measured by balance, positive forward, N

$F_{A,mom}$ momentum tare axial force due to bellows, N

F_g gross thrust, N (see appendix)

F_i ideal isentropic gross thrust, N (see appendix)

F_j thrust along body axis, N

h_t geometric throat height for wedge nozzle 1 (fig. 5)

$\dot{m}_i$ ideal mass-flow rate, kg/sec

$\dot{m}_p$ measured mass-flow rate, kg/sec

N_{bal} resultant normal force measured by balance, N

N_j jet normal force, N

p_a ambient pressure, Pa

p_{ch} chamber pressure, Pa

$p_{t,j}$ average jet total pressure, Pa

R gas constant (for $\gamma = 1.3997$), 287.3 N-m/kg-K

$T_{t,j}$ jet total temperature, K

x,y coordinates of nozzle internal and external surfaces (fig. 6), cm

x_e,y_e coordinates of nozzle exit, cm

x_n longitudinal coordinate of leading edge of convergent flap for 2-D C-D/1 nozzle (fig. 9)

$x_s,y_{s,1},y_{s,2}$ coordinates of sidewall for 2-D C-D/2 nozzle (fig. 11)

x_t,y_t coordinates of nozzle throat, cm

β_w wedge half-angle, deg

γ ratio of specific heats, 1.3997 for air

Δ increment

δ effective jet turning angle, deg

δ_v geometric turning angle, deg

Subscripts:

f location of geometric throat on boattail flap for wedge nozzle 1 (fig. 5)

w location of geometric throat on wedge for wedge nozzle 1 (fig. 5)

1 location of upper divergent flap exit of 2-D C-D nozzle at vectoring (fig. 9)

2 location of lower divergent flap exit of 2-D C-D nozzle at vectoring (fig. 9)

Abbreviations:

ASME	American Society of Mechanical Engineers
C-D	convergent-divergent
DPR	design pressure ratio
FS	fuselage station, cm
int	intermediate power setting
max	maximum power setting
NPR	nozzle pressure ratio, $p_{t,j}/p_a$
2-D	two-dimensional

BASIC FLOW APPARATUS AND PROCEDURE

Twin-Jet Propulsion Simulation System

A sketch of the twin-jet propulsion simulation system is presented in figure 1. This propulsion simulation system was also used in the investigations described in references 8 and 9. Photographs of the simulation system in the static-test stand of the Langley 16-foot transonic tunnel are presented in figure 2. The body shell forward of FS 132.08 cm was removed for the static tests.

An external high-pressure air system provides a continuous flow of clean, dry air at a controlled temperature of about 306 K at the nozzle. This high-pressure air is brought through the support strut by six tubes into a high-pressure chamber. (See fig. 1.) Here the air is divided into two separate flows and is passed through flow-control valves. These manually operated valves are used to balance the exhaust-nozzle total pressure in each duct. As shown in figure 3, the air in each supply pipe is then discharged perpendicularly to the model axis through eight sonic nozzles equally spaced around the supply pipe. This method is designed to eliminate any forces imposed by the transfer of axial momentum as the air is passed from nonmetric to the metric portion of the model. The metric portion of the model is that mounted to the force balance. Two flexible metal bellows are used as seals and serve to compensate for the axial forces caused by pressurization. The cavity between the supply pipe and bellows is vented to model internal pressure. The tailpipes are connected to the thrust balance whose loads are then transmitted to the main balance through the wing and thrust-balance support block. (See fig. 1.)

The air is then passed through the tailpipes to the exhaust nozzles as shown in figure 1. An enlargement section, choke plate, flow straightener, and instrumentation section are attached to the tailpipes at FS 122.44 cm for the base-line axisymmetric nozzles as shown in figure 4. The three nozzle geometries representing different engine power settings are all attached at FS 137.16 cm. For the nonaxisymmetric-nozzle concepts, a common transition, instrumentation, and choke-plate section were used as indicated in figure 1.

Static-Test Facility and Instrumentation

This investigation was conducted in the static-test facility of the Langley 16-foot transonic tunnel. This facility is used for a variety of purposes such as determination of nozzle static performance or initial calibration of new propulsion simulation systems prior to installation in the 16-foot transonic tunnel. Testing is accomplished in a room with a high ceiling where the jet exhausts to the atmosphere through a large open doorway. The control room is remotely located from the test area, and a closed-circuit television camera is used to observe the model. This facility utilizes the same clean, dry-air supply and a similar air-control system, including valving, filters, and heat exchanger (to operate the jet flow at constant stagnation temperature) as used in the 16-foot transonic tunnel. The static-test facility also has a similar 100-channel, magnetic-tape data-acquisition system.

Nozzle internal forces were measured by both a main force balance and the thrust balance. (See fig. 1.) However, only those forces measured by the main force balance are presented herein. (See the appendix.) A turbine flowmeter was used to measure total mass flow to both nozzles. In addition, the pressure and temperature in each supply pipe were measured prior to discharge of the flow through the eight sonic nozzles in order to determine mass-flow rate to each nozzle. The discharge coefficients of the sonic nozzles are determined by using calibration nozzles. These flow measurements were used independently to check the mass-flow rate as determined from the turbine flowmeter. The two mass-flow measurements were generally within 1/2 percent of each other. Flow conditions in each nozzle were determined from measurements of total pressure and temperature made at FS 129.5 cm. For the axisymmetric nozzle, total pressure was measured by a single probe, whereas four probes were used in each nozzle duct for the nonaxisymmetric nozzles. All pressures were measured with individual pressure transducers, and temperatures were measured with iron-constantan thermocouples.

Nozzle total-pressure surveys were made during separate calibration runs by translating a shielded total-pressure probe (Kiel tube) across the flow duct in the instrumentation sections for both the axisymmetric (fig. 4) and nonaxisymmetric nozzles (fig. 1). These surveys were made at approximately the same fuselage station as that of the total-pressure probes that were installed in the instrumentation sections. Surveys were made along the nozzle center-line vertical plane for the axisymmetric nozzle and along both the nozzle horizontal and vertical planes for the nonaxisymmetric nozzles. The three generic-type nonaxisymmetric nozzles were surveyed at flow rates corresponding to the three power settings in each duct in order to determine any effects of nozzle-throat geometrical differences on the distortion of the total pressure at the measuring station. For the nozzles with lower flow rates, the numerically averaged total pressure (from total-pressure probes in instrumentation section) was within 0.2 percent of the integrated value. For the nozzles with the high flow rate, the results were mixed and somewhat dependent upon throat geometry with as much as 2-percent differences between the average and integrated total pressure. However, the numerical average was used since the maximum pressure ratio which could be tested at static conditions for these nozzles was well below the nozzle nominal operating pressure ratio.

NOZZLE DESIGNS

One axisymmetric and five nonaxisymmetric nozzles based upon full-scale concepts were tested. The five nonaxisymmetric nozzles represented three generically different types: (1) two-dimensional wedge or plug with combined internal-external expansion, (2) two-dimensional convergent-divergent design (2-D C-D), and (3) a single-expansion ramp with combined internal-external expansion.

The nozzle designs were based on the following guidelines. Nozzle-throat area and internal-expansion area ratios were sized to be consistent with advanced mixed-flow turbofan engine cycles. Three power settings for each basic nozzle concept were provided and they simulated the following:

(1) Dry power: Cruise condition, typically a Mach number from 0.80 to 0.90.

(2) Intermediate power: Maximum afterburning at subsonic speeds, typically the subsonic maneuver point at a Mach number of 0.90.

(3) Maximum power: Maximum afterburning at supersonic speeds, typically Mach numbers greater than 1.5.

The ratio of total nozzle-throat area to body maximum cross-sectional area was also consistent with current twin-engine fighter airplanes. The nozzle geometric and sizing parameters are summarized in table I. The duct upstream of the nozzle throat was square. All the nonaxisymmetric nozzles had square corners in the duct downstream of the choke plate. A close-spaced buried engine installation was chosen for the nozzle integration scheme. The interfairing between the nozzles resulted from providing for remote actuation of thrust vectoring for two of the nozzles.

Base-Line Axisymmetric Nozzle

The base-line axisymmetric nozzle shown in figure 4 simulates an advanced technology axisymmetric convergent-divergent (C-D) design with fully variable area-ratio control. In the full-scale design, optimum area ratio is provided for all operating pressure ratios up to 9.3 (maximum area ratio of 2.0). By comparison, the maximum area ratio for the C-D nozzle of a current fighter airplane is 1.55 which is optimum for a pressure ratio of approximately 6.0.

Wedge Nozzle 1

This fixed- (noncollapsing) wedge nozzle incorporates a variable-incidence plug and is shown in figure 5. It employs a pair of load-balanced boattail flaps which are rotated to set throat area and internal area ratio simultaneously. A 12° half-angle, two-piece wedge is utilized to control thrust-vector angle by programmed differential rotation of the two wedge segments about a common hinge location. This rotation scheme results in a redistribution of flow at the throat, increasing the percentage of flow through the lower throat passage,

and simultaneously canting the lower throat plane in the desired vectoring direction. The flow turning through the lower throat (combined subsonic turning and supersonic shock deflection) is more effective than the upper throat mechanism (supersonic expansion turning). Thus, vectoring effectiveness should be improved when compared to a design without rotation of the forward-wedge segment.

For the model design, the wedge was remotely actuated to provide continuous vectoring over a range from -30° to 30° of tail flap rotation for all three power settings. The wedge was hinged and linked by the actuation system such that the tail flap moved 2° for each 1° rotation of the forward-wedge segment.

Wedge Nozzle 2

The collapsing wedge nozzle 2, shown in the sketches of figure 6 and in the photographs of figure 7, was designed to accomplish reversing at dry power and vectoring at all power settings. This nozzle was a modified version of that tested in reference 6. The original design incorporated a boattail shroud with pure axial translation for internal area-ratio control. The translating shroud was changed to a translating-rotating shroud to provide additional area ratio in the maximum power mode. The transition section upstream of the throat was also changed by eliminating corner radii to accommodate model installation requirements, although the basic area distribution was retained. Thrust vectoring is achieved in this concept with a "double-hinged" wedge to provide minimum loss through supersonic expansion turning on the upper surface and supersonic deflection turning on the lower surface. Sidewall size was minimized in the interest of avoiding weight and cooling penalties. Thrust reversing was obtained by deploying flaps out of the wedge upper and lower surfaces for the dry-power setting.

Two-Dimensional Convergent-Divergent Nozzle 1

The mechanical features of the first two-dimensional convergent-divergent nozzle (2-D C-D/1) are shown in figure 8. Details and a photograph of the model tested are shown in figure 9. This nozzle utilizes rotary-convergent flap actuation for jet area control and independent rotary actuation of the external boattail flaps for area ratio and vectoring control. The divergent flaps follow the boattail flaps through a sliding joint mechanism. The thrust reverser is integral to the primary convergent flaps. The upstream end of the flaps unport to form the reverse-flow exhaust path (fig. 8). A cutback sidewall geometry was utilized to reduce nozzle weight and cooled surface area. A short divergent flap design was selected for this 2-D C-D/1 nozzle to minimize weight and cooling requirements at the expense of reduced area ratio ($A_e/A_t = 1.28$ at intermediate power with a divergence angle of 12°). Test results will permit tradeoffs to be made in weight, cooling, and internal performance between the design approaches for this and the other 2-D C-D nozzle concept of this investigation. Further design information including detailed mechanical features, estimated weights, and cooling required for this 2-D C-D/1 nozzle and the two wedge nozzles can be found in reference 12.

Two-Dimensional Convergent-Divergent Nozzle 2

The mechanical features of the second two-dimensional convergent-divergent nozzle (2-D C-D/2) are shown in figure 10. Details and a photograph of the model tested are shown in figure 11. The full-scale design would allow independent actuation of the convergent area control flaps and the divergent flaps, thus providing control of area ratio and thrust-vector angle independent of throat area. The design employs long divergent flaps to achieve a maximum internal area ratio of 1.6 and, therefore, should provide good supersonic internal performance. The sidewalls of this nozzle were also cut back to reduce weight and cooling requirements. The full-scale nozzle would incorporate a variable-geometry sidewall as indicated in figure 11. A thrust reverser was also provided for this nozzle.

Single-Expansion Ramp Nozzle

The single-expansion ramp-type nozzle has a two-dimensional single-expansion ramp which results in combined internal-external expansion. This concept is a derivative of the augmented deflector exhaust nozzle of reference 10. The model tested, which is shown in the sketches of figure 12 and the photographs of figure 13, features elliptical throat and expansion surface cross sections. In the model, the elliptical contours have been approximated by a "race-track" shaped flow path formed by semicircular and straight-line segments. Throat area and internal area ratio are set by an adjustable lower surface boattail flap and sidewall spacers, simulating rotation of the area control flap. In the full-scale nozzle, the rotating lower flap is actually part of a swiveling pressure vessel with a continuous structure that proceeds up the sidewalls and through a pressurized cavity in the fixed-geometry upper expansion ramp structure. This design innovation reduces actuation forces and maintains structurally efficient hoop stress in the area control flap. In the model, thrust vectoring is controlled by remote actuation of the external-expansion flap. This feature permitted finding the exact optimum-thrust-vector-angle settings in both positive and negative directions.

TESTS

The investigation was conducted in the static-test facility of the Langley 16-foot transonic tunnel. All five nonaxisymmetric models and the base-line axisymmetric model were tested over a range of nozzle pressure ratios up to the model-facility airflow limits. All six nozzle models were tested at three power settings and various thrust-vectoring—thrust-reversing positions. Reverser test configurations were fabricated and tested for three nozzle models. Vectoring configurations were tested at only the intermediate power setting, representative of maximum afterburning operation at subsonic maneuvering conditions, for the two 2-D C-D models. Dry-power vectoring configurations of these nozzles were not fabricated. A summary of the nozzle configurations tested is presented in table I. A summary of the various calibrations performed is given in the appendix.

RESULTS AND DISCUSSION

The variation of ideal thrust coefficient with nozzle pressure ratio for the three power settings tested is presented in figure 14. Ideal thrust coefficient can be used to obtain thrust levels from the basic performance parameter F_g/F_i which is the ratio of measured resultant or gross thrust to ideal thrust. Unvectored static performance characteristics for the base-line axisymmetric nozzles are presented in figure 15. Both unvectored and vectored static performance characteristics for the five nonaxisymmetric nozzles are given in figures 16 to 26.

Summary of Unvectored Performance

A comparison of unvectored static performance of all the nozzles tested is presented in figure 27. The results indicate that dry-power nozzle performance is at two separate levels depending upon the generic nozzle type at the nominal operating pressure ratio of 3.5. For the higher performance level, the performance of the two 2-D C-D nozzles, which are internal-expansion-type nozzles, is essentially the same as that of the base-line axisymmetric nozzle. The performance of the three nozzles with external-expansion surfaces was 2.0 to 2.3 percent lower than the axisymmetric-nozzle level. However, recompression effects of external flow on the external-expansion surface generally have a beneficial effect of increasing internal performance at forward velocities. This positive incremental thrust force is usually enough to overcome the lower internal static performance, especially at Mach numbers greater than 0.8. This is illustrated in reference 6 for a single-wedge nozzle and in reference 8 for a twin-wedge nozzle configuration.

For the intermediate power setting, four of the five nonaxisymmetric nozzles had performance within 1 percent of the base-line axisymmetric nozzle at or near the nominal operating pressure of 5.0. The performance of the wedge nozzle 1 was approximately 2 percent less than that of the axisymmetric nozzle. However, this performance is still considered to be competitive with the other nozzle designs. No conclusions can be reached with regard to the nozzles at maximum power setting because the test NPR was considerably lower than the nominal operating pressure ratio of 7.0. The wide variation in performance at the test power setting is due to overexpansion losses for the nozzles with $A_e/A_t = 1.60$ (except for wedge nozzles). Peak performance will occur at a lower pressure ratio for the nozzles with the low area ratios than for the nozzles with the high area ratios.

It should be noted that the performance presented in figure 27 for the single-expansion ramp nozzle is for a zero vector angle. It was possible with this nozzle to determine the flap vector angle which resulted in maximum internal performance by remotely actuating the external-expansion flap (fig. 12). This was done only for the dry- and intermediate-power settings, by maximizing balance axial force at NPR = 3.5 or 5.0 depending upon power setting. A pressure-ratio sweep was then made at the fixed-geometric vector angle δ_v determined in this manner. These angles were $\delta_v = -6^\circ$ for dry power and $\delta_v = -5^\circ$ for the intermediate power settings. As shown in figure 22, increases in internal performance were obtained, especially for the dry-power setting. At

$\delta_v = 0^o$, the jet exhaust is apparently overdeflected by the expansion flap. The negative vector angles required for maximum internal performance eliminate an undesirable flow-decelerating interference with the exhaust expansion and provide effective overall area ratios which result in an increased exit momentum (ref. 11). However, with the negative-thrust-vector angles an undesirable negative normal force is produced, which would cause a nose-up airplane moment.

A comparison of the static performance of the wedge nozzles from the present investigation with those from references 6 to 8 is presented in figure 28 for dry-power nozzle settings only. At pressure ratios greater than 3, the two wedge nozzles of the present investigation had up to 1.3 percent higher performance than the wedge nozzle of reference 6 and up to 1.8 percent higher performance than the wedge nozzle of reference 7 with $A_e/A_t = 1.05$. Note, however, that wedge nozzle 1 and the wedge nozzle of reference 6 peaked in performance at NPR ≈ 2.75 which is a typical take-off nozzle pressure ratio. The static performance for the wedge nozzle of reference 8 is presented for reference only. Its performance is lower at the low values of NPR as a result of overexpansion losses caused by an internal area ratio which is too large for static conditions.

Also shown in figure 28 is static dry-power performance for several wedge nozzles with different wedge half-angles. Wedge half-angle can be increased in order to shorten the overall length of the wedge and hence lighten the structural weight and reduce the surface area to be cooled. However, increasing the wedge half-angle above 12^o to 13^o can lead to a substantial decrease in static performance (for example, see alternate nozzle of ref. 8), and can decrease performance at forward speeds (refs. 8 and 13).

All the nozzles of figure 28, except wedge nozzle 1, vary throat area by collapsing the wedge. The minimum wedge height of the nozzle is dependent upon the actuation system that can be housed within the collapsed wedge for the maximum power setting. This usually includes the vectoring and reversing mechanisms. Wedge nozzle 1, on the other hand, has a fixed wedge with rotating boattail flaps used for throat-area variation. Thus, boattail angle can be traded against maximum wedge height and wedge angle for a fixed nozzle aspect ratio in order to shorten wedge length. Consequently, by having this additional freedom to reduce wedge height, a substantial decrease in wedge length can be achieved. For example, the wedge height of wedge nozzle 1 is 21.7 percent less than the wedge height of wedge nozzle 2 (2.542 cm to 1.99 cm), and the wedge is 41.4 percent shorter which results in reduced surface area. It is probably because of this reduced surface area that the performance of wedge nozzle 1 is higher than that of the wedge nozzle of reference 7 with $\beta_w = 13.3^o$.

It should be noted that only in the investigation of reference 7 was nozzle geometry varied parametrically. For these nozzles, the wedge half-angle downstream of the nozzle exit was varied. Three wedges with $A_e/A_t = 1.10$ and wedge angles of 8^o, 10^o, and 13.3^o were tested. Wedge length varied from -16.5 to 16.5 percent from the base-line 10^o wedge. Static performance for the 8^o wedge was essentially equal to the 10^o wedge and hence was not shown. As indicated in reference 13, wedge length has a significant effect on performance at forward speeds. For the shorter 13.3^o wedge, a loss of up to 2 percent was found at a Mach number of 0.90.

Static Vectored Performance

One of the potential benefits identified for nonaxisymmetric nozzles in prior studies (refs. 2 and 3) was supercirculation lift due to thrust vectoring. However, this potential for improved maneuvering capabilities can be easily offset by losses in nozzle internal performance associated with thrust vectoring. For example, the results of reference 8 show that a loss in static performance of about 3 to 4 percent for $\delta_v = 24^o$ resulted in a 30- to 40-percent loss in thrust-minus-drag performance at a Mach number of 0.90. The analytical study of reference 3 indicates that 15^o vectoring is optimum for subsonic maneuver and that losses in performance of more than 2 percent at $\delta = 15^o$ would substantially negate any supercirculation benefits. High-vectored internal performance is, therefore, a requirement if the maneuver enhancement potential provided by thrust vectoring is to be realized.

Each of the five nonaxisymmetric-nozzle concepts of this investigation has a thrust-vectoring range up to 30^o. Several different thrust-vectoring mechanisms for exhaust flow turning were represented. Both 2-D C-D nozzle concepts vector thrust by independent actuation of the upper and lower divergent flaps which results in nearly subsonic flow turning through a skewed throat. The single-expansion ramp-nozzle concept achieves positive vectoring through supersonic-flow deflection of the exhaust flow and negative vectoring through supersonic expansion turning over the vectoring flap.

Wedge nozzle 2 combines supersonic deflection on the lower wedge surface with supersonic expansion turning on the upper wedge surface. The forward portion of this wedge is fixed and the first vectoring hinge line on the wedge is downstream of the nozzle exit. (See fig. 6.) Wedge nozzle 1, by rotating the forward wedge section, combines some supersonic expansion turning with efficient subsonic flow turning upstream of the nozzle throat. For this nozzle concept, the proportion of efficient subsonic flow turning to supersonic expansion turning increases with increasing vector angle.

Static vectoring performance for the five nonaxisymmetric nozzles is presented in figures 17 to 26. Shown is the variation of the performance parameter F_g/F_i and effective turning angle δ with nozzle pressure ratio. The data are summarized in figure 29 where geometric turning angle δ_v and an incremental performance parameter $\Delta F_g/F_i$ are shown varying with the effective turning angle δ. Note that the incremental performance parameter is defined as

$$\frac{\Delta F_g}{F_i} = \left(\frac{F_g}{F_i}\right)_{\delta_v} - \left(\frac{F_g}{F_i}\right)_{\delta_v=0^o}$$

Positive vectoring.- In general, the relative merit of the various nozzle concepts at positive vectoring conditions is strongly dependent upon the type of flow turning employed. For example, figure 29 indicates that at the nominal operating pressure ratio of 3.50, for the dry-power setting, the three nozzles tested have essentially complete flow turning ($\delta_v \approx \delta$). However, there is no performance loss for the wedge nozzle 1 which has essentially subsonic flow turning with up to 88 percent of the exhaust flow passing through the lower

throat of the nozzle. As pressure ratio increases there is a small gain in internal performance. The two nozzles that employ supersonic deflection turning (wedge nozzle 2 and the single-expansion ramp) have large decrements in performance that exceed the 2-percent-loss criterion of reference 3 at vector angles above 12°. The turning effectiveness $(\delta < \delta_v)$ of the wedge nozzle 2 decreased as pressure ratio increased, probably due to separation over the upper portion of the wedge. Turning equal to or greater than the geometric vector angle is desired from a mechanical standpoint since less actuator travel would be required for a given effective turning angle.

The single-expansion ramp nozzle on the other hand exhibits an increase in turning effectiveness with increasing pressure ratio but with larger performance losses as high as 7.5 percent. These performance losses are related to shock-induced momentum losses resulting from the supersonic-flow-turning process and some sidewall spillage (ref. 11). Note that the effective turning angle can be larger than the geometric vector angle since it is the effective direction of the force vector produced by a combination of exit momentum and a pressure-area force felt by the fixed and rotating external-expansion surfaces.

The static vectoring performance of the nozzles at the intermediate power setting (fig. 29(b)) shows the same dependence on the type of flow turning as do those at the dry-power setting. At the intermediate setting, all the nonaxisymmetric nozzles were tested and the two 2-D C-D nozzles had the best overall vectoring performance with no turning losses because of their subsonic flow turning. These nozzles exhibit an increase in effective turning which probably results from a pressure gradient between the upper and lower divergent flaps (creating a positive normal force). This pressure gradient, due to the large turning angle around the lower flap, causes an overexpansion which does not fully recompress on the lower divergent flap (ref. 11). The vectored thrust performance of the 2-D C-D/1 nozzle is somewhat lower than that of the 2-D C-D/2 nozzle (fig. 29(b)) because of a shorter divergence flap which limits recompression over this flap. The maximum decrement in performance is about 1.2 percent which is still less than the 2-percent criterion of reference 3.

In figure 30 the static vectoring performance of the wedge nozzles of the present investigation is compared with that of reference 8. The wedge nozzle of reference 8, which also had a double-hinged wedge for vectoring, had a smaller performance decrement due to vectoring than the wedge nozzle 2. The better vectoring performance of the nozzle of reference 8 may be due to the location of the first hinge line relative to the nozzle exit. The first hinge line of the wedge nozzle of reference 8 is located at the nozzle-exit plane and, thus, the first turn that the flow will negotiate may be at a lower supersonic Mach number than for the wedge nozzle 2 where the hinge line is located downstream of the exit. Thus, the shock-induced momentum loss may be less due to a reduced supersonic Mach number.

Negative vectoring.- The single-expansion ramp nozzle (fig. 12) was also tested at negative-thrust-vector angles, which requires supersonic expansion turning entirely for flow turning. Figures 23(b), 24(b), and 25(b) show the variation of F_g/F_i and δ with nozzle pressure ratio for constant settings of flap vector angle. Because this nozzle was remotely actuated, it is possible to obtain data over a varying range of vector angle and, hence, effective

turning at constant nozzle pressure ratio. These results are shown in figure 26 for the intermediate power setting. The aforementioned data are then summarized in figure 29.

The results of figure 29 show that maximum static internal performance of the single-expansion ramp nozzle is generally obtained between effective turning angles of -5° and -10°. There is generally a sharp decrease in performance as the flap vector angles exceed -16°. At $\delta_v = -16^{\circ}$, the external ramp and vectoring flap form a continuous surface. When the vectoring flap is at angles between -16° and -24°, the flow must negotiate a convex corner and there is most likely a tendency for the flow to separate from the flap and cause a decrease in performance.

Thrust-Reversing Performance

Significant potentials for improved deceleration capabilities at all flight conditions were identified in the analytical study of reference 3 for an assumed reverse thrust of 30 percent of the forward thrust. However, for landing operation, reverse-thrust levels of 50 percent of the forward thrust are desirable for effective ground-roll reduction. Thus, a 50-percent reversal in thrust level will be used to judge the thrust-reverser concepts tested.

Thrust-reverser performance for the three nozzle concepts tested is presented in figure 31. The 2-D C-D/2 nozzle meets or exceeds the aforementioned goal over most of the nozzle pressure-ratio range tested. The reverse-thrust levels were only 10 to 25 percent of forward thrust for both the 2-D C-D/1 nozzle and wedge nozzle 2. However, neither of these two configurations had full sidewalls to contain the flow. This can be seen by the sketches in figures 6, 8, and 9. During the tests, the exhaust flow at reverse conditions was known to spread laterally because instrumentation lines were blown away at the model sides. Addition of larger sidewalls to the wedge nozzle 2 would probably increase the reverse-thrust levels to that measured in reference 8 which had full sidewalls. However, the full extent of sidewalls needed may be configuration oriented since the reversed exhaust flow at forward speeds can have sizable detrimental effects on stability and control effectiveness (ref. 8).

CONCLUSIONS

An investigation has been conducted in the static-test facility of the Langley 16-foot transonic tunnel to determine the static performance of five twin-engine nonaxisymmetric nozzles and a base-line axisymmetric nozzle at three nozzle power settings. Static thrust-vectoring and thrust-reversing performance were also determined. Nonaxisymmetric-nozzle concepts included two-dimensional convergent-divergent nozzles, wedge nozzles, and a nozzle with a single external-expansion ramp. Thrust vectoring for the various concepts was accomplished by subsonic turning, supersonic shock deflection, supersonic expansion turning, or some combination of these, depending on the nozzle concept. The results of this investigation indicate the following conclusions:

1. The two-dimensional convergent-divergent nozzles had essentially the same performance as that of the base-line axisymmetric nozzle. For the dry- or cruise-power setting at the nozzle design pressure ratio of 3.5, the nozzles with external-expansion surfaces had a lower performance than the axisymmetric nozzle by 2.0 to 2.3 percent.

2. Thrust-vectoring performance was highly dependent upon the type of flow turning employed. Those nozzles that used only subsonic turning had essentially no turning losses due to thrust vectoring up to 30° deflection. The nozzle with supersonic shock deflection (single-expansion ramp nozzle) had the lowest performance with losses as high as 7.5 percent.

3. One two-dimensional convergent-divergent nozzle achieved a reverse-thrust level of 50 percent of the forward thrust. Two other configurations had reverse-thrust levels of 10 to 25 percent of the forward thrust. However, these two nozzle configurations may have greater reverse-thrust levels by the use of full sidewalls to contain the flow.

Langley Research Center
National Aeronautics and Space Administration
Hampton, VA 23665
May 31, 1978

APPENDIX

DATA-REDUCTION AND CALIBRATION PROCEDURE

Internal nozzle forces were measured by both the main and thrust balance (fig. 1). For a wind-tunnel investigation with external flow, the main force balance would measure total lift, thrust-minus-axial force, and total pitching moment of the entire model aft of FS 99.06 cm. The thrust balance will sense nozzle internal normal and axial forces and external forces on that portion of the model aft of FS 132.08 cm which is the metric break between the thrust and main force balance. For the current investigation at static conditions, both balances measure nozzle internal forces only. However, only those forces measured by the main balance have been presented herein.

Because the center line of the force balances is located above and below the jet center line (fig. 1), a force and moment interaction exists between the bellows-flow transfer system (fig. 3) and the force balances. Consequently, single and combined calibration loadings of normal and axial force and pitching moment were made. In addition, loads were applied to the model with the jets operating with ASME type calibration nozzles shown in figure 32. The calibrations with the jets operating were performed because this condition gives a more realistic effect of pressurizing the bellows than does capping off the nozzles and pressurizing the flow system. However, loadings were also done in the axial-force direction with the flow system capped off and pressurized, and this method indicated no effect on the axial force measured by the main balance. Thus, in addition to the usual balance-interaction corrections applied for a single force balance under combined loads, another set of interactions were made to the data from this investigation for the combined loading effect of the balance with the bellows system. These calibrations were performed over a range of expected normal force and pitching moment. The interactions can be determined by either single or combined loadings.

The corrected jet axial force F_j and jet normal force N_j are then computed by the following equations:

$$F_j = F_{A,bal} + K_1 N_{bal} + K_2 - F_{A,mom}$$

$$N_j = K_3 + K_4 N_{bal} + K_5 N_{bal} p_{ch} + K_6 p_{ch}$$

where $F_{A,bal}$ and N_{bal} are measured balance forces and K_1 to K_6 are constants obtained from the calibration. The momentum tare axial force $F_{A,mom}$, which ideally should be zero, is a momentum tare correction and is a function of the average bellows internal pressure which is a function of the internal chamber pressure p_{ch} in the supply pipes just ahead of the sonic nozzles (fig. 3). At an internal supply pressure of 1380 kPa (corresponding to $p_{t,j}/p_a \approx 4.0$), this tare is approximately 5 percent of the maximum static thrust, and its repeatability is 0.25 percent of the maximum static thrust. This tare results from high internal velocities in the bellows area where the flow is being ejected radially. This condition causes a pressure differential to exist between the ends of the bellows. The momentum tare force was deter-

mined from calibrations prior to and after the tests with the standard calibration nozzles shown in figure 32.

The iris-convergent nozzles of reference 14 were also tested to ascertain whether this tare was invariant with nozzle-throat area because of the large difference in throat area between the dry-power and afterburner-power nozzle settings for the current investigation. The results indicated no effect of variation of throat area on this tare force.

From the measured axial and normal components of the jet resultant force, determined at static conditions for each vectored nozzle configuration, the nozzle gross thrust and effective jet turning angle are defined, respectively, as

$$F_g = \sqrt{F_j^2 + N_j^2}$$

and

$$\delta = \tan^{-1} \frac{N_j}{F_j}$$

The total ideal isentropic gross thrust or exhaust jet momentum for both nozzles is

$$F_i = \dot{m}_p \sqrt{RT_{t,j} \frac{2\gamma}{\gamma - 1} \left[1 - \left(\frac{p_a}{p_{t,j}} \right)^{(\gamma-1)/\gamma} \right]}$$

where $\dot{m}_p$ is the mass-flow rate measured by the turbine flowmeter and $p_{t,j}$ is the average jet stagnation pressure for both nozzles. The average jet total pressure $p_{t,j}$ is determined by numerically averaging the total number of individual measurements made.

The ideal isentropic gross thrust of each nozzle can also be determined if the mass-flow rate for each nozzle is known. The eight sonic nozzles forward of each of the nozzle tailpipes can be used for measuring mass flow by determining their effective discharge coefficients (ref. 9).

A summary of the calibrations on the twin-jet propulsion simulation system conducted prior to the investigations of references 8 and 9 and during the present investigation is presented in table II. A summary of the performance characteristics of the twin-jet propulsion simulation system with the calibration nozzles installed is presented in figure 33. Also included are performance characteristics for a similar type of nozzle from reference 15. These results indicate excellent repeatability during each particular study and

excellent agreement between investigations. Figure 34 presents a comparison of the performance obtained during the present investigation for the iris-convergent nozzles (shown in fig. 32) with the performance obtained during investigations reported in references 8 and 14. This comparison indicates good agreement for the iris-convergent nozzles with the two largest throat areas. The performance for the nozzle with $A_t = 16.82$ cm^2 (dry power) measured during the investigation of reference 14 is 1/2 to 1 percent higher than the other data.

REFERENCES

1. Martens, Richard E.: F-15 Nozzle/Afterbody Integration. J. Aircr., vol. 13, no. 5, May 1976, pp. 327-333.

2. Capone, Francis J.: Summary of Propulsive-Lift Research in the Langley 16-Ft Transonic Tunnel. J. Aircr., vol. 13, no. 10, Oct. 1976, pp. 803-808.

3. Hiley, P. E.; Wallace, H. W.; and Booz, D. E.: Nonaxisymmetric Nozzles Installed in Advanced Fighter Aircraft. J. Aircr., vol. 13, no. 12, Dec. 1976, pp. 1000-1006.

4. Sedgwick, T. A.: Investigation of Nonaxisymmetric Two-Dimensional Nozzles Installed in Twin-Engine Tactical Aircraft. AIAA Paper No. 75-1319, Sept.-Oct. 1975.

5. Berrier, Bobby L.; Palcza, J. Lawrence; and Richey, G. Keith: Nonaxisymmetric Nozzle Technology Program - An Overview. AIAA Paper 77-1225, Aug. 1977.

6. Maiden, Donald L.: Performance of an Isolated Two-Dimensional Variable-Geometry Wedge Nozzle With Translating Shroud and Collapsing Wedge at Speeds Up to Mach 2.01. NASA TN D-7906, 1975.

7. Maiden, Donald L.: Performance of an Isolated Two-Dimensional Wedge Nozzle With Fixed Cowl and Variable Wedge Centerbody at Mach Numbers Up to 2.01. NASA TN D-8218, 1976.

8. Capone, Francis J.; and Maiden, Donald L.: Performance of Twin Two-Dimensional Wedge Nozzles Including Thrust Vectoring and Reversing Effects at Speeds Up to Mach 2.20. NASA TN D-8449, 1977.

9. Capone, Francis J.: The Effects on Propulsion-Induced Aerodynamic Forces of Vectoring a Partial-Span Rectangular Jet at Mach Numbers From 0.40 to 1.20. NASA TN D-8039, 1975.

10. Lander, J. A.; Nash, D. O.; and Palcza, J. Lawrence: Augmented Deflector Exhaust Nozzle (ADEN) Design for Future Fighters. AIAA Paper No. 75-1318, Sept.-Oct. 1975.

11. Willard, C. M.; Capone, F. J.; Konarski, M.; and Stevens, H. L.: Static Performance of Vectoring/Reversing Non-Axisymmetric Nozzles. AIAA Paper 77-840, July 1977.

12. Stevens, H. L.: F-15/Nonaxisymmetric Nozzle System Integration Study Support Program. NASA CR-135252, 1978.

13. Maiden, Donald L.; and Petit, John E.: Investigation of Two-Dimensional Wedge Exhaust Nozzles for Advanced Aircraft. J. Aircraft, vol. 13, no. 10, Oct. 1976, pp. 809-816.

14. Mercer, Charles E.; and Berrier, Bobby L.: Effect of Afterbody Shape, Nozzle Type, and Engine Lateral Spacing on the Installed Performance of a Twin-Jet Afterbody Model. NASA TM X-1855, 1969.

15. Holdhusen, James S.; and Lamb, Owen P.: Scale Model Studies of Exhaust Nozzle Performance. AIAA Paper No. 66-641, June 1966.

TABLE I.- NOZZLE SIZING AND STATIC-TEST SUMMARY

(a) Nozzle sizing

Power setting	A_t, cm^2	$2A_t/A_{max}$	Nominal operating NPR
Dry	15.677	0.11	3.5
Intermediate . . .	27.032	0.19	5.0
Maximum	33.290	0.23	7.0

(b) Static-test summary

Type of nozzle	A_t, cm^2	A_e/A_t	DPR	Range of δ_v, deg	Reverser
Axisymmetric	15.677	1.15	3.46	0	
	27.032	1.30	4.65	0	
	33.290	1.60	7.12	0	
Wedge nozzle 1	15.677	1.06	2.72	0 to 30	
	27.032	1.20	3.86	0 to 30	
	33.290	1.28	4.49	0 to 30	
Wedge nozzle 2	15.677	1.15	3.46	0 to 30	✓
	27.032	1.25	4.25	0 to 30	
	33.290	1.32	4.79	0 to 30	
2-D C-D/1	15.677	1.10	3.05	0	✓
	27.032	1.28	4.49	0 to 20	
	33.290	1.28	4.49	0	
2-D C-D/2	15.677	1.15	3.46	0	✓
	27.032	1.27	4.41	0 to 30	
	33.290	1.60	7.12	0	
Single-expansion ramp	15.677	1.15	3.46	-24 to 28	
	27.032	1.21	3.94	-24 to 28	
	33.290	1.27	4.39	-24 to 28	

TABLE II.- SUMMARY OF CALIBRATION TESTS

Investigation	Nozzle	A_t, cm^2	Total NPR sweeps	Test location
Present study	Calibration	30.190	8	Static stand
	Iris convergent	16.836	2	Static stand
	Iris convergent	41.969	2	Static stand
	Calibration	30.190	12	Wind tunnel
	Iris convergent	16.836	6	Wind tunnel
	Iris convergent	30.288	3	Wind tunnel
	Iris convergent	41.970	3	Wind tunnel
Reference 9	Calibration	30.190	6	Static stand
	Calibration	30.190	2	Wind tunnel
Reference 8	Calibration	30.190	8	Wind tunnel
	Iris convergent	16.836	5	Wind tunnel
	Iris convergent	30.288	5	Wind tunnel
	Iris convergent	41.970	9	Wind tunnel

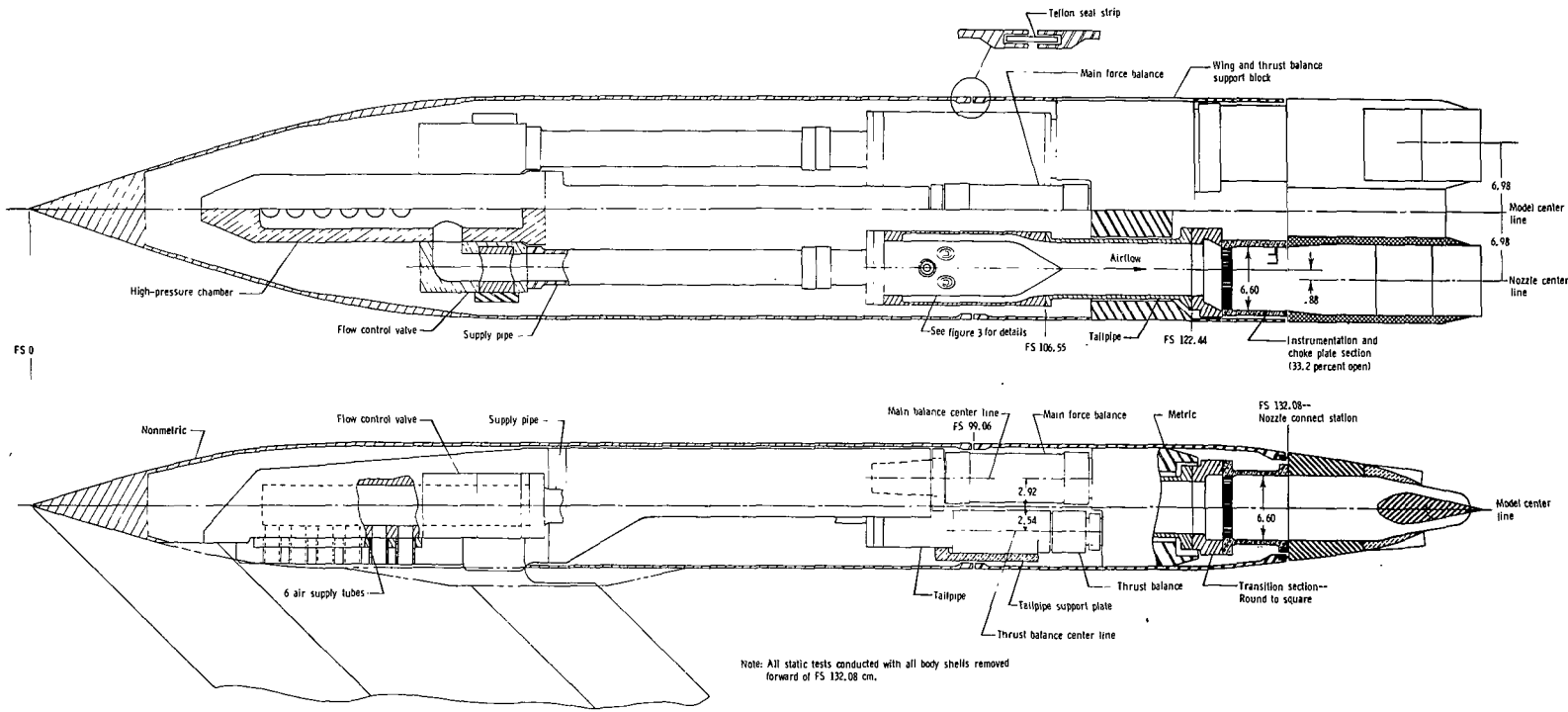

Figure 1.- Sketch of twin-jet propulsion simulation system. Nozzle lateral spacing shown is same for nonaxisymmetric nozzles. All dimensions are in centimeters unless otherwise noted.

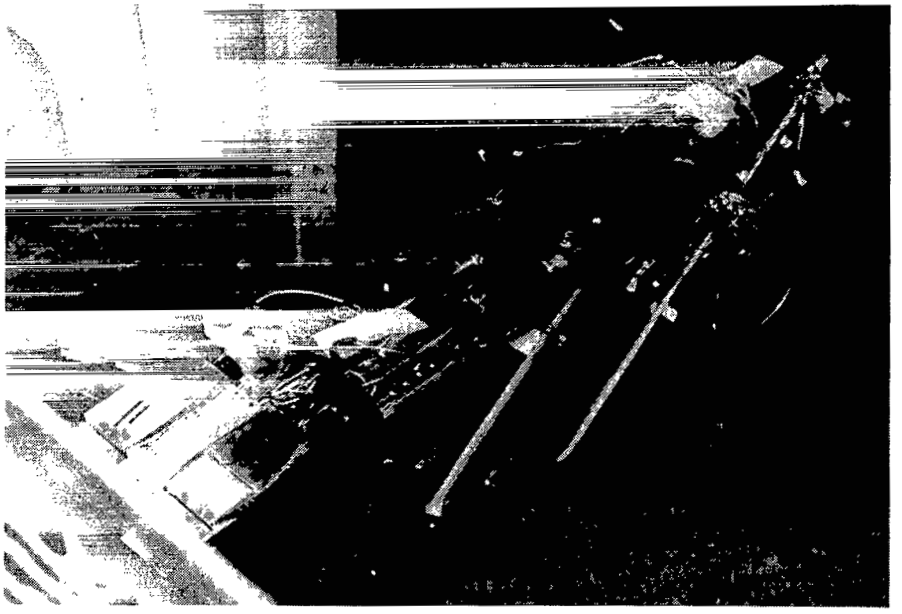

L-77-973

(a) Top view.

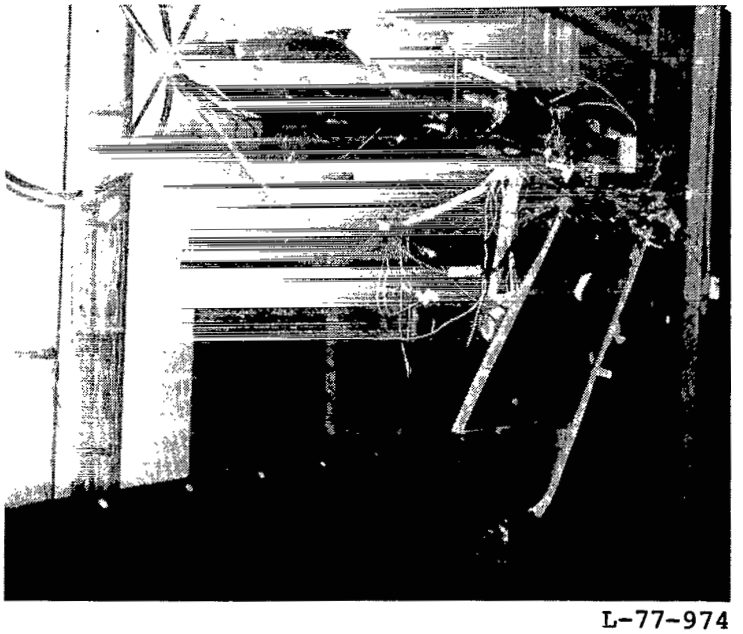

L-77-974

(b) Rear view.

Figure 2.- Photographs of test setup.

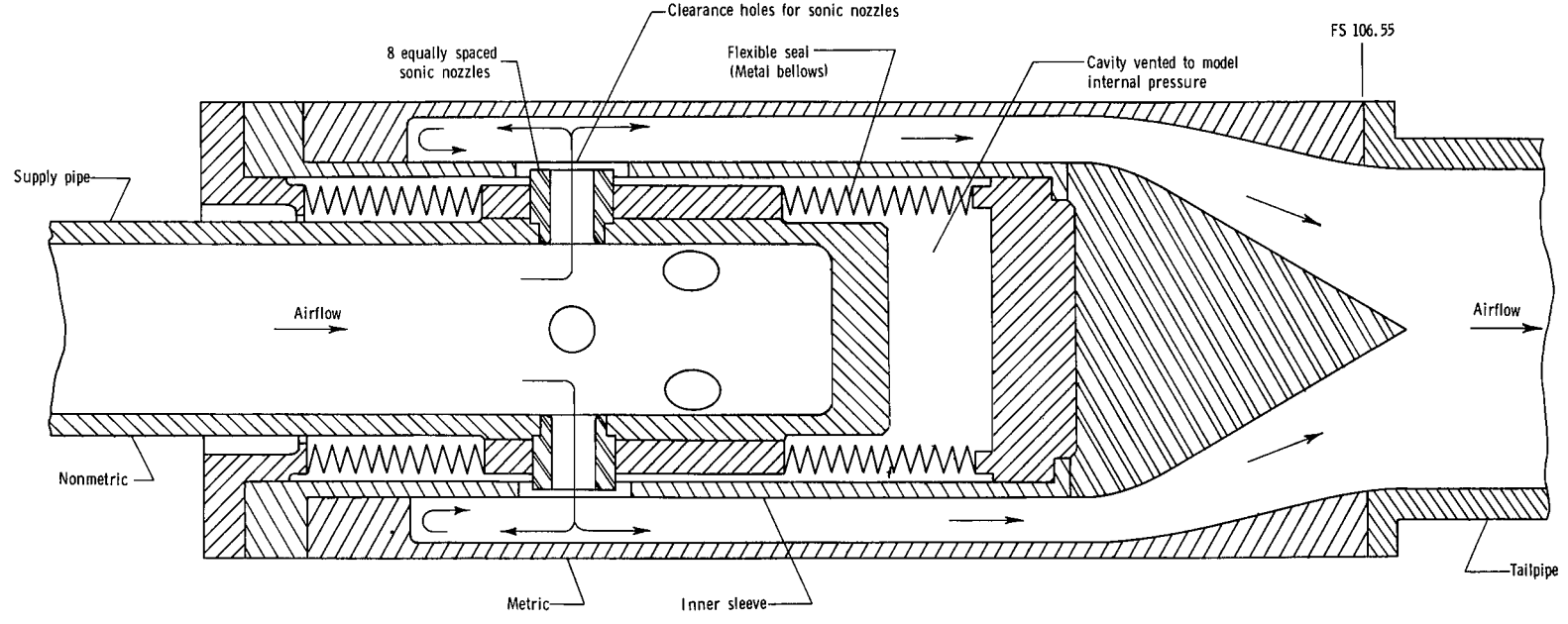

Figure 3.- Details of bellows arrangement used to transfer air from nonmetric to metric portions of model.

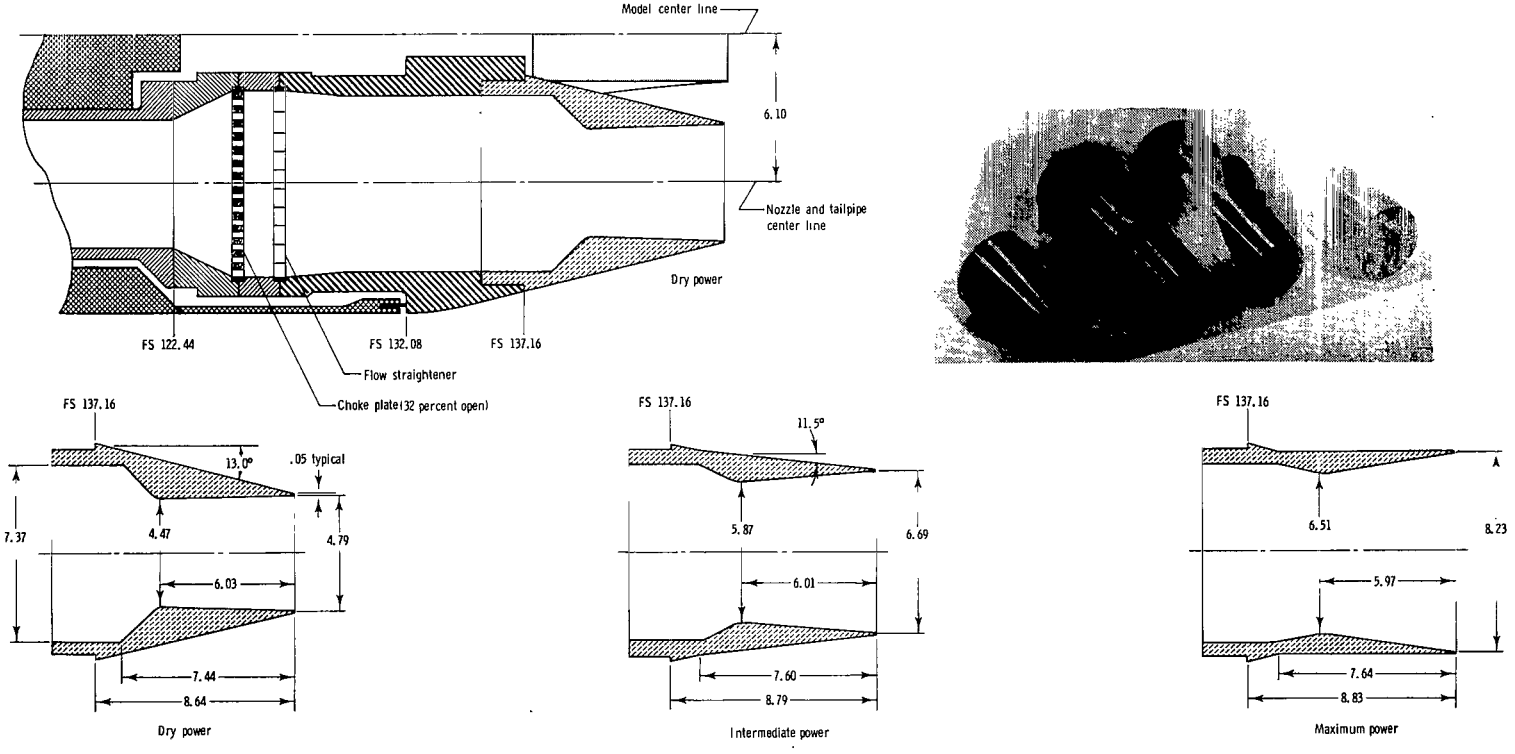

L-77-1110

Figure 4.- Details and photographs of base-line axisymmetric nozzles. All dimensions are in centimeters unless otherwise noted.

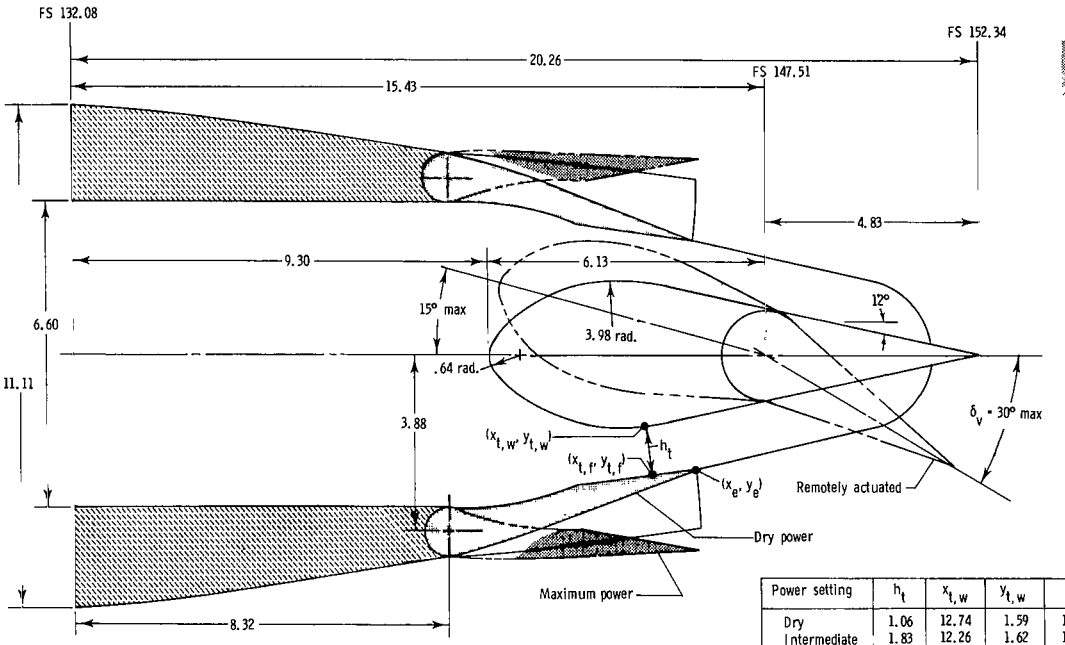

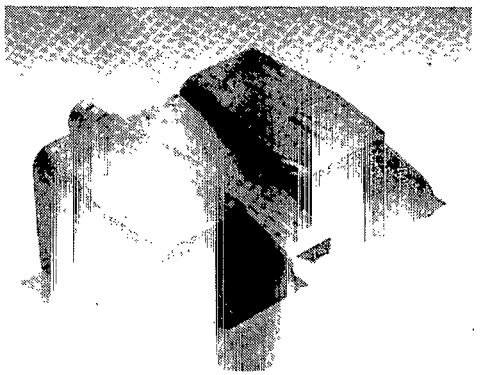

Power setting	h_t	$x_{t,w}$	$y_{t,w}$	$x_{t,f}$	$y_{t,f}$	x_e	y_e
Dry	1.06	12.74	1.59	12.87	2.59	13.82	2.51
Intermediate	1.83	12.26	1.62	11.97	3.40	13.90	3.50
Maximum	2.26	11.72	1.59	11.40	3.48	13.97	4.22

L-77-1113

Figure 5.- Details and photographs of wedge nozzle 1. Nozzle has diverging sidewalls from FS 132.08 to FS 135.89; nozzle width from FS 135.89 to exit is 7.37 cm. All dimensions are in centimeters unless otherwise noted.

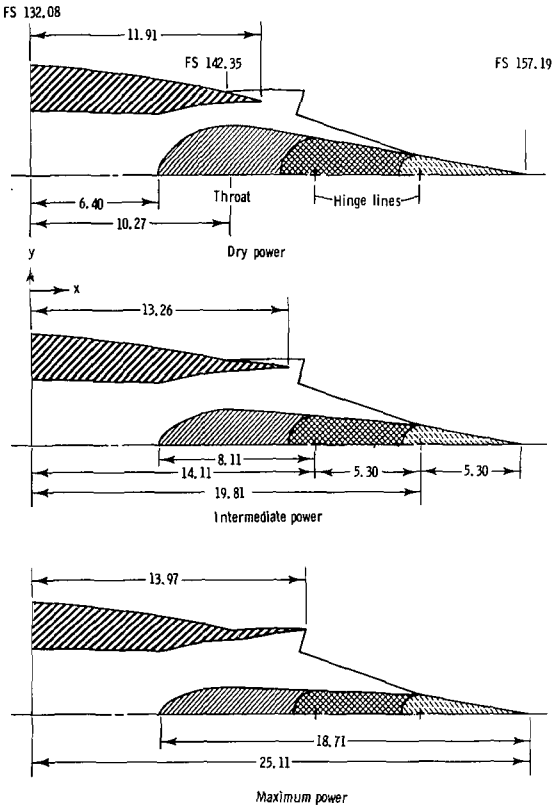

Wedge coodinates			
	Power setting		
	Dry	Int	Max
x	y	y	y
6.40	0.000	0.000	0.000
6.70	.673	.470	.356
7.00	1.016	.709	.538
7.40	1.364	.952	.724
7.80	1.641	1.146	.871
8.20	1.872	1.306	.993
8.60	2.068	1.443	1.095
9.00	2.233	1.557	1.184
9.40	2.367	1.651	1.255
9.80	2.471	1.725	1.311
10.27	2.542	1.773	1.349
14.51	1.842	1.460	1.173
19.81	.952	.952	.952
25.12	0.000	0.000	0.000
throat radius	5.085	3.546	2.698

Wall coodinates			
	Power setting		
	Dry	Int	Max
x	y	y	y
0.000	3.302		
6.40	3.104		
6.70	3.104		
7.00	3.157		
7.40	3.246		
7.80	3.368		
8.20	3.475		
8.60	3.531		
9.00	3.589		
9.40	3.594		
9.80	3.597		
10.27	3.607	3.607	3.607
11.04	3.645	3.645	3.645
11.91	3.683	3.683	3.683
12.56	--	3.810	3.937
13.26	--	3.912	4.242
13.58	--	--	4.318
13.97	--	--	4.369

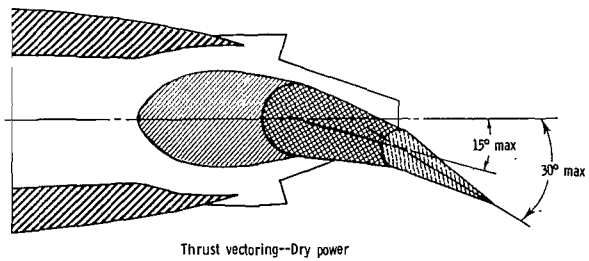

Thrust vectoring--Dry power

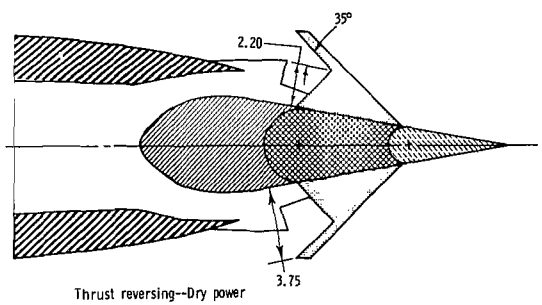

Thrust reversing--Dry power

Figure 6.- Details of wedge nozzle 2. Nozzle has diverging sidewalls from FS 132.08 to FS 135.89; nozzle width from FS 135.89 to exit is 7.37 cm. Wall coordinates are identical up to x = 10.27 for three power settings. All dimensions are in centimeters unless otherwise noted.

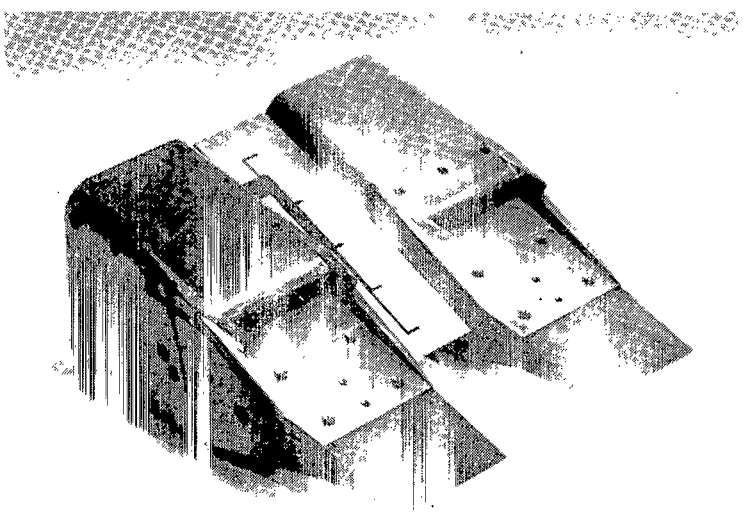

L-77-1112

(a) Without thrust reverser.

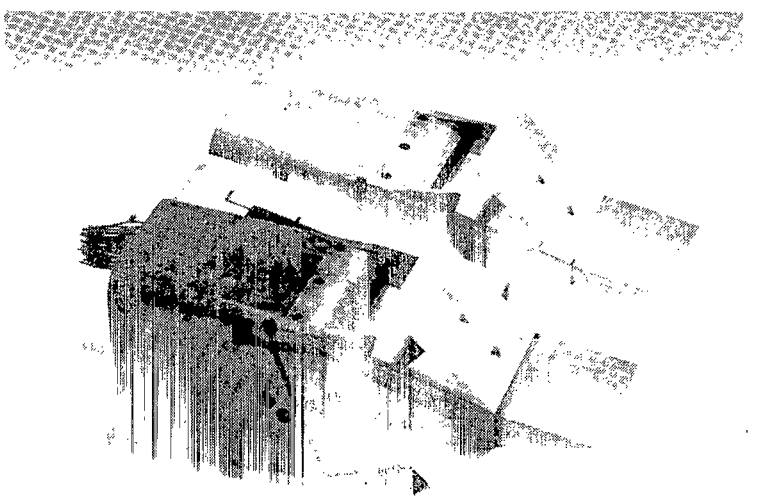

L-77-1122

(b) With thrust reverser.

Figure 7.- Photographs of wedge nozzle 2.

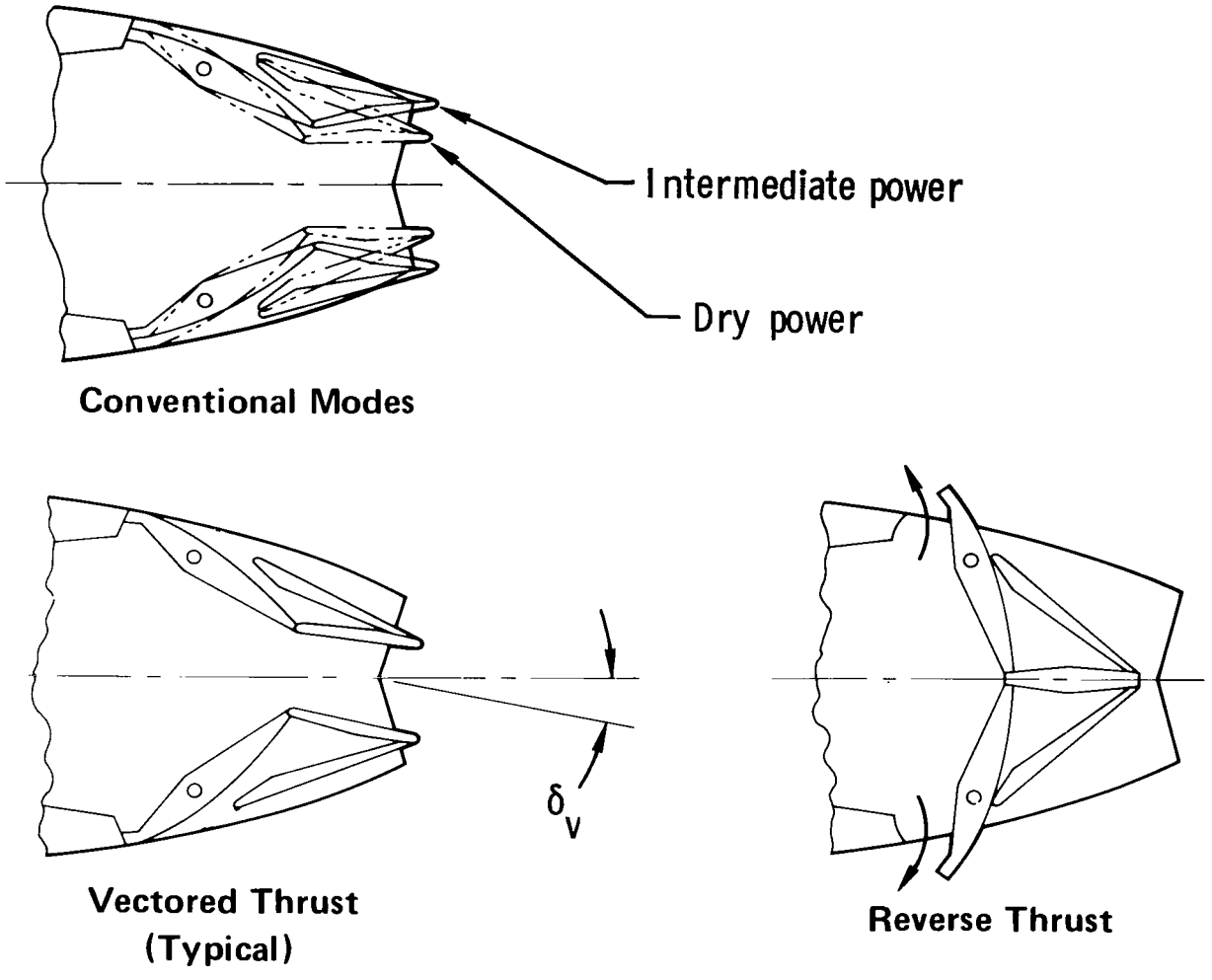

Figure 8.- Mechanical features of the 2-D C-D/1 nozzle.

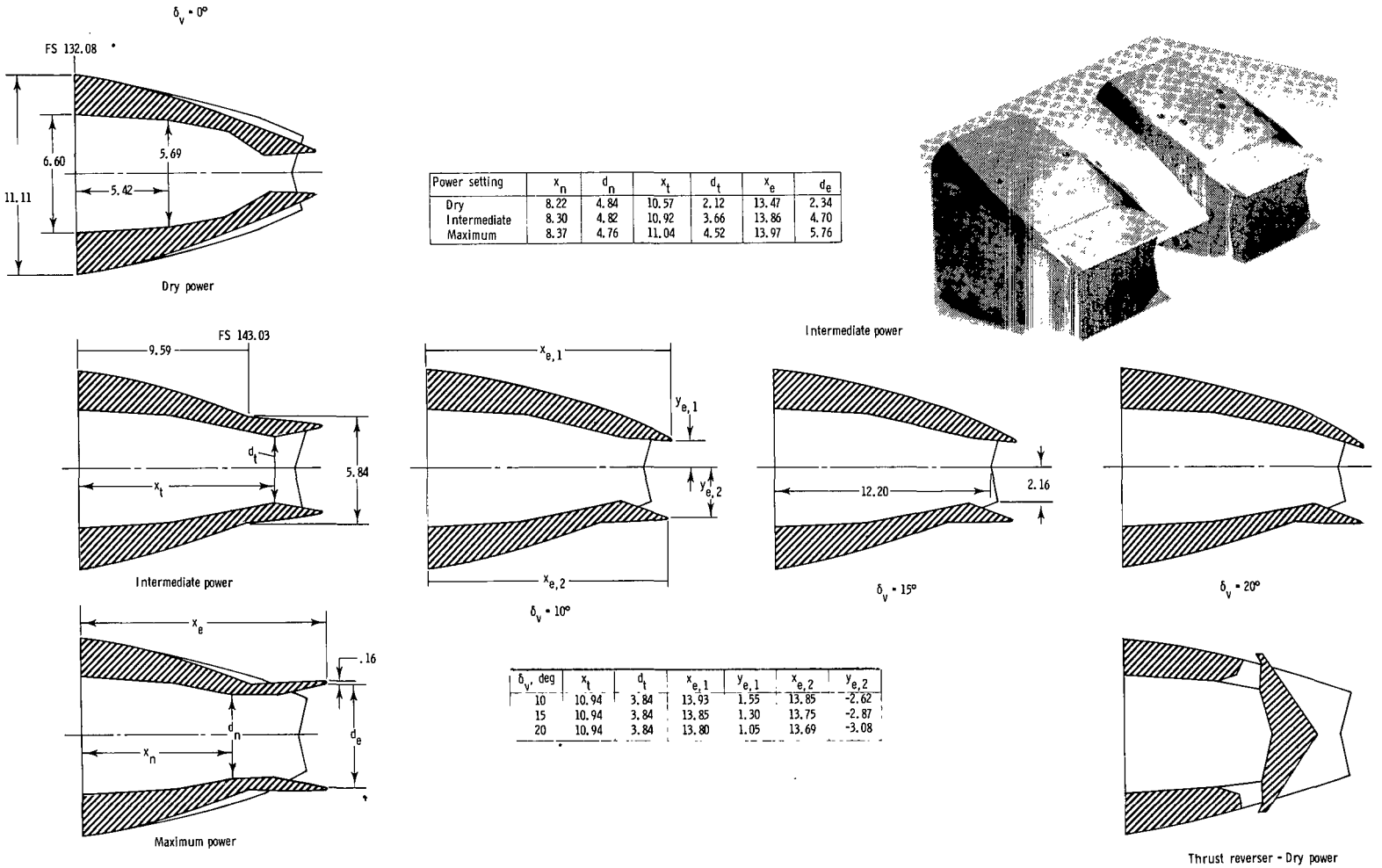

Power setting	x_n	d_n	x_t	d_t	x_e	d_e
Dry	8.22	4.84	10.57	2.12	13.47	2.34
Intermediate	8.30	4.82	10.92	3.66	13.86	4.70
Maximum	8.37	4.76	11.04	4.52	13.97	5.76

δ_v, deg	x_t	d_t	$x_{e,1}$	$y_{e,1}$	$x_{e,2}$	$y_{e,2}$
10	10.94	3.84	13.93	1.55	13.85	-2.62
15	10.94	3.84	13.85	1.30	13.75	-2.87
20	10.94	3.84	13.80	1.05	13.69	-3.08

L-77-1123

Figure 9.- Details and a photograph of the 2-D C-D/1 nozzle. Nozzle has diverging sidewalls from FS 132.08 to FS 135.89; nozzle width from FS 135.89 to exit is 7.37 cm. All dimensions are in centimeters unless otherwise noted.

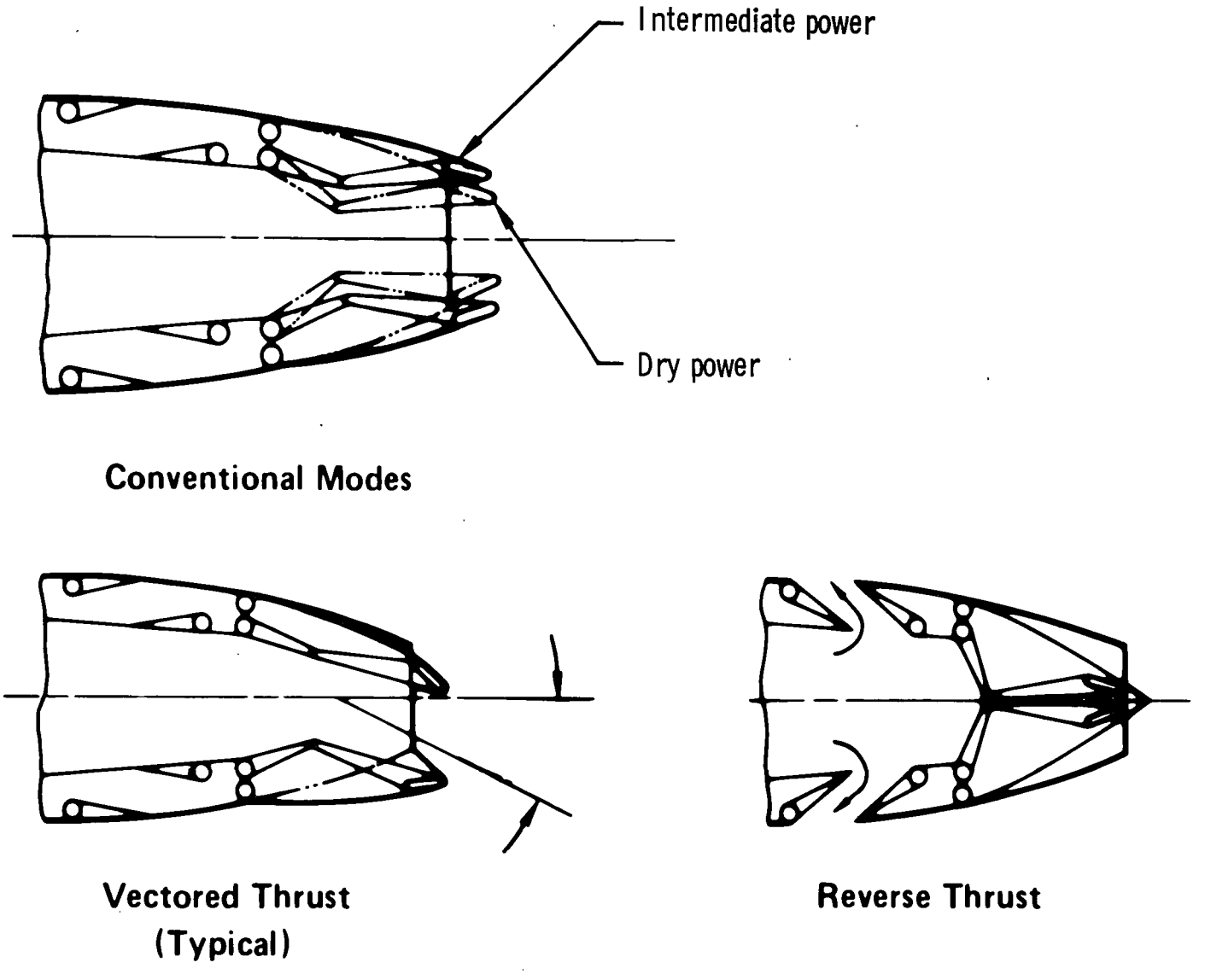

Figure 10.- Mechanical features of the 2-D C-D/2 nozzle.

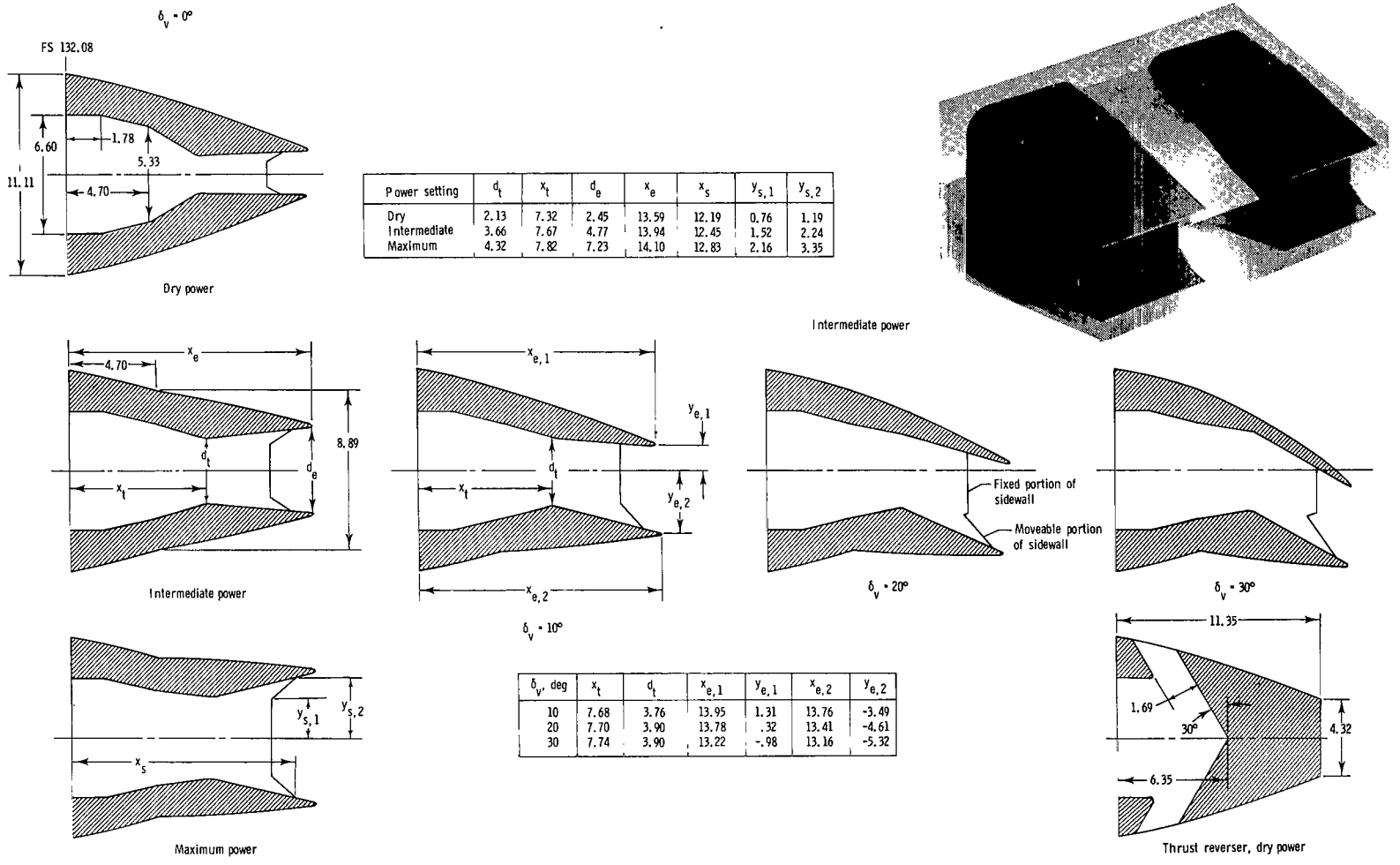

Power setting	d_t	x_t	d_e	x_e	x_s	$y_{s,1}$	$y_{s,2}$
Dry	2.13	7.32	2.45	13.59	12.19	0.76	1.19
Intermediate	3.66	7.67	4.77	13.94	12.45	1.52	2.24
Maximum	4.32	7.82	7.23	14.10	12.83	2.16	3.35

δ_v, deg	x_t	d_t	$x_{e,1}$	$y_{e,1}$	$x_{e,2}$	$y_{e,2}$
10	7.68	3.76	13.95	1.31	13.76	-3.49
20	7.70	3.90	13.78	.32	13.41	-4.61
30	7.74	3.90	13.22	-.98	13.16	-5.32

L-77-1118

Figure 11.- Details and a photograph of the 2-D C-D/2 nozzle. Nozzle has diverging sidewalls from FS 132.08 to FS 135.89; nozzle width from FS 135.89 to exit is 7.37 cm. All dimensions are in centimeters unless otherwise noted.

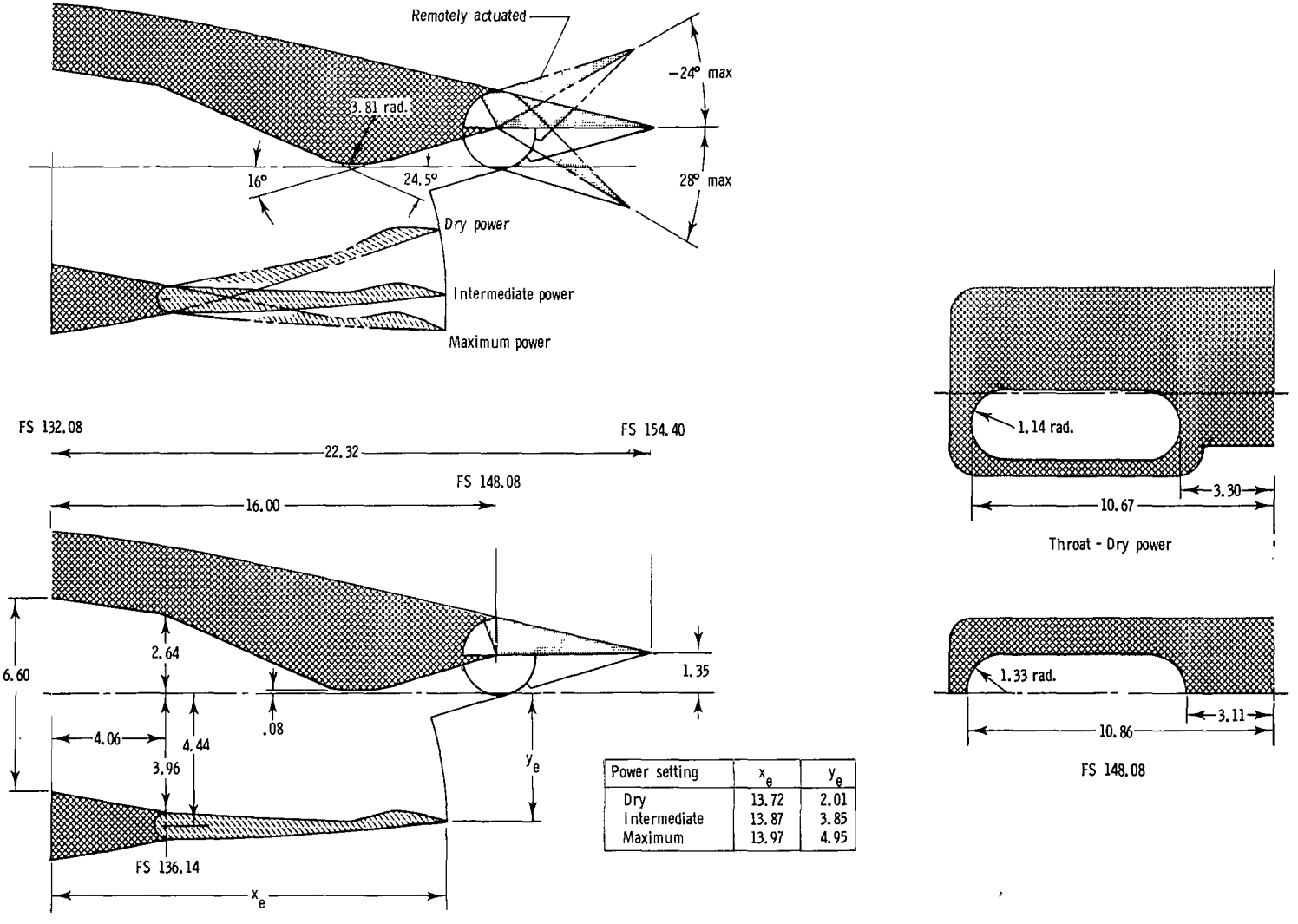

Power setting	x_e	y_e
Dry	13.72	2.01
Intermediate	13.87	3.85
Maximum	13.97	4.95

Figure 12.- Details of single-expansion ramp nozzle. All dimensions are in centimeters unless otherwise noted.

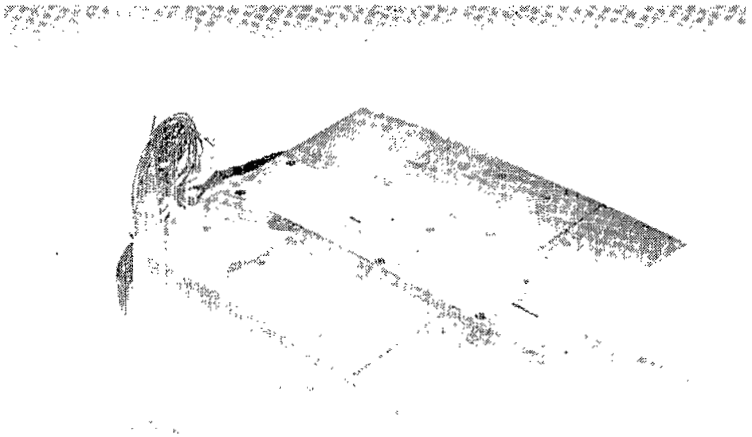

L-77-1120

(a) Top view.

L-77-1124

(b) Bottom view.

Figure 13.- Photographs of single-expansion ramp nozzle.

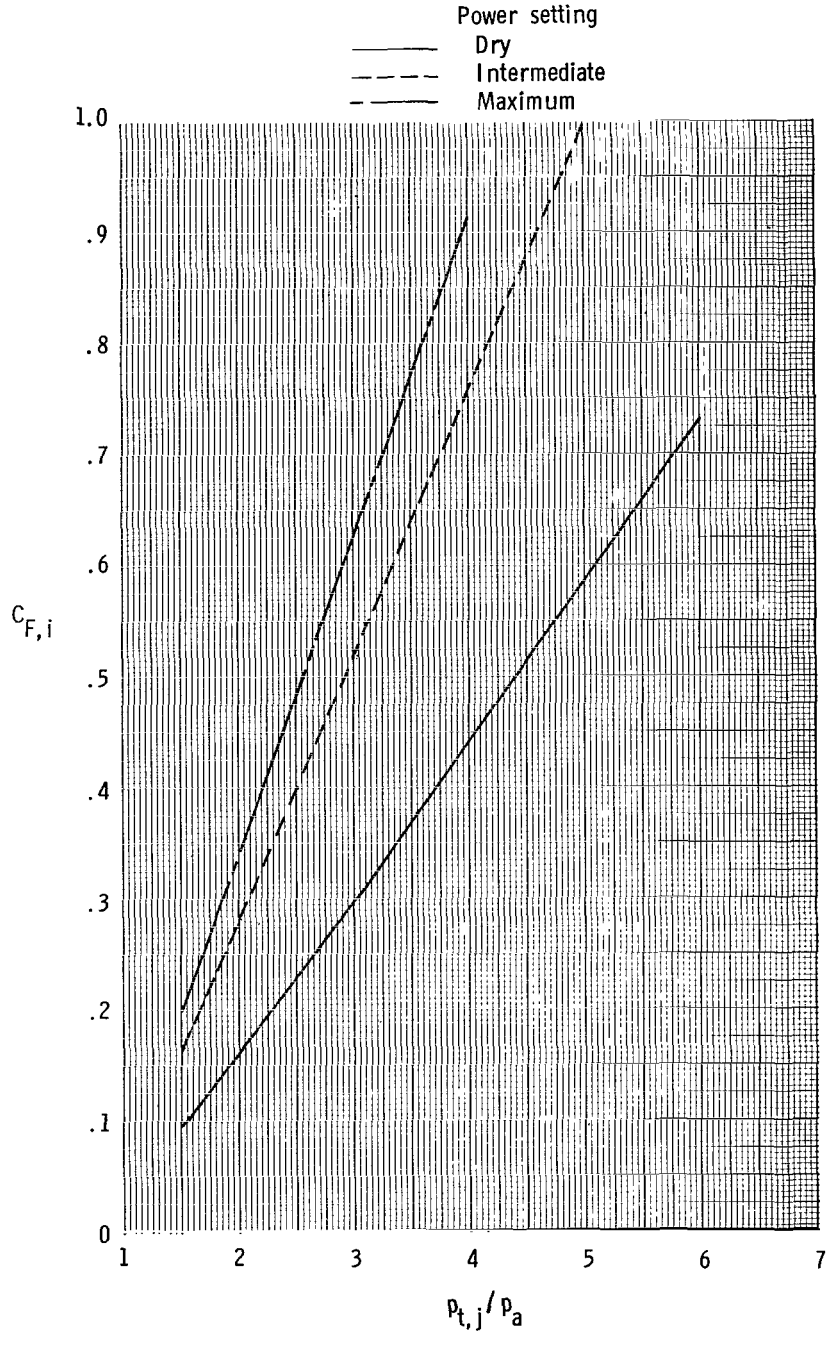

Figure 14.- Variation of ideal thrust coefficient with nozzle pressure ratio.

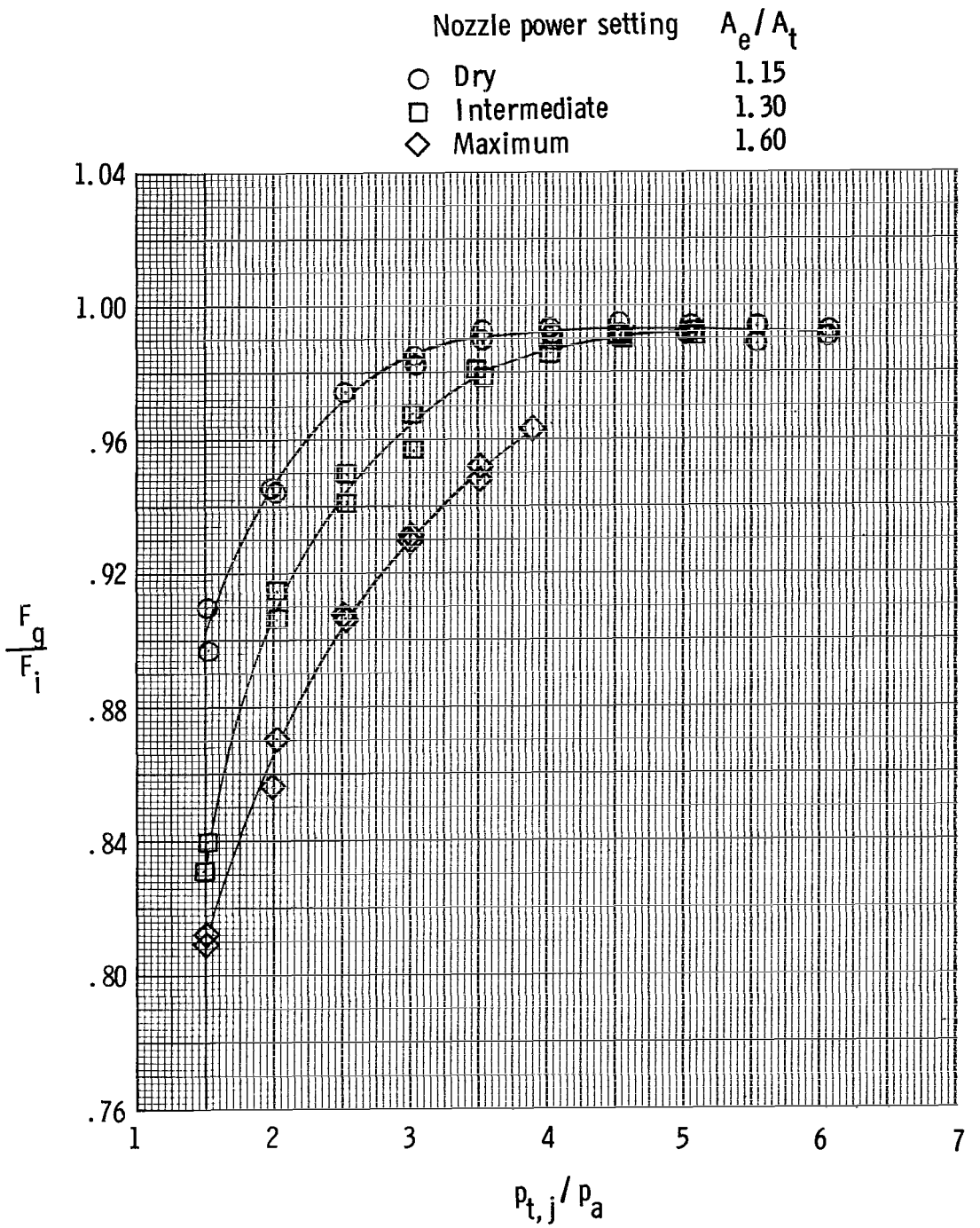

Figure 15.- Unvectored static performance characteristics of axisymmetric nozzles.

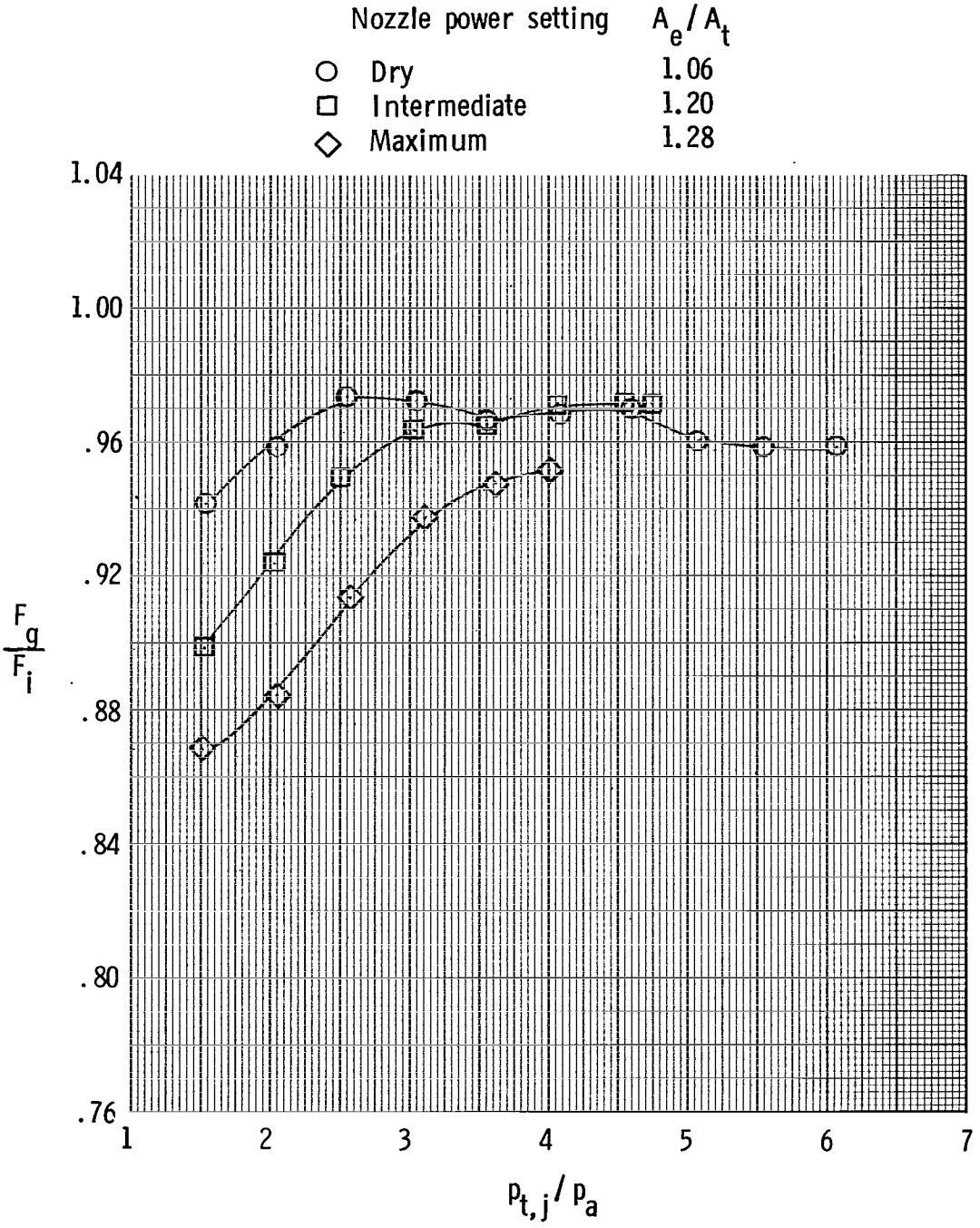

Figure 16.- Static performance characteristics of wedge nozzle 1.

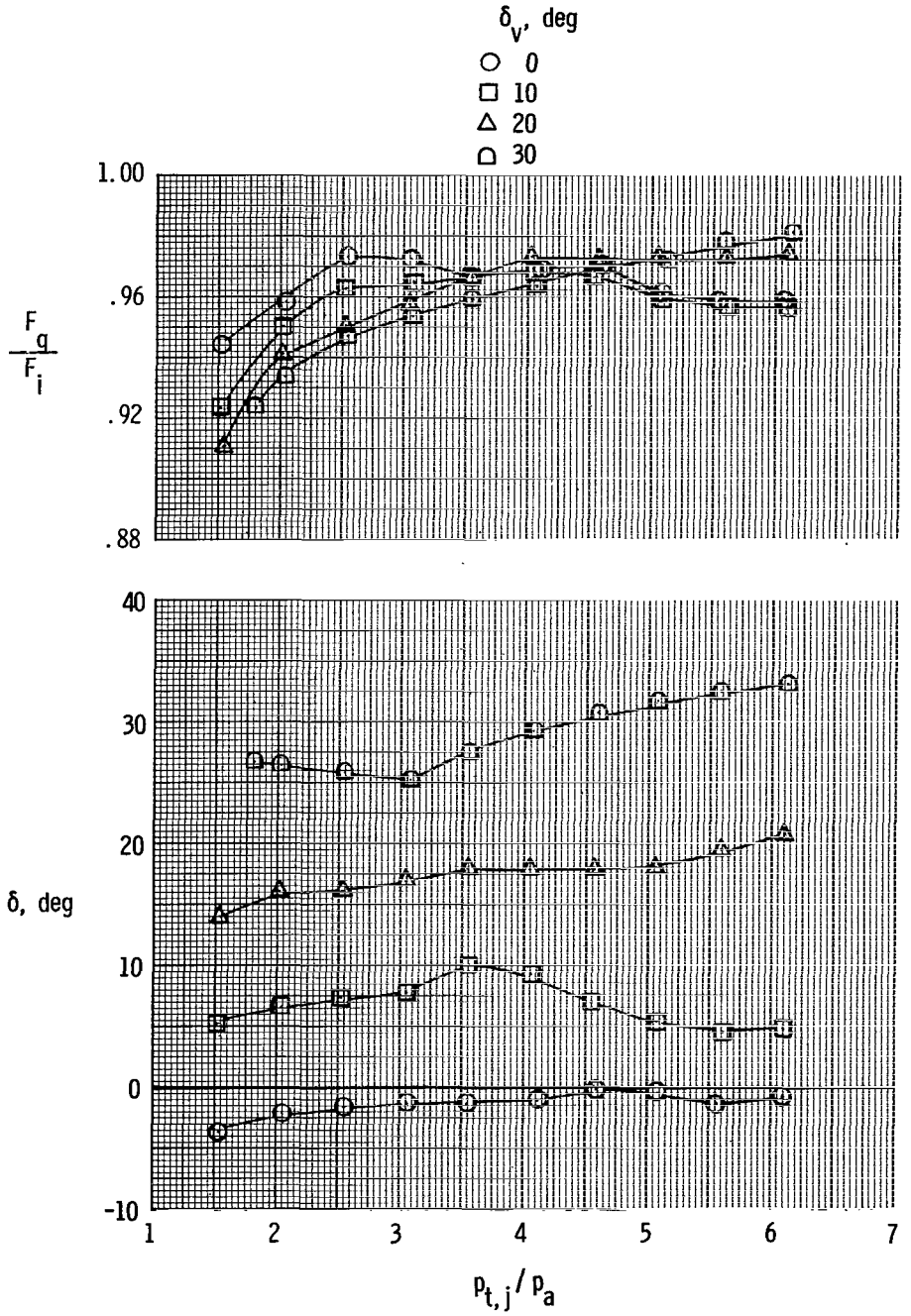

(a) Dry power.

Figure 17.- Static vectoring performance of wedge nozzle 1.

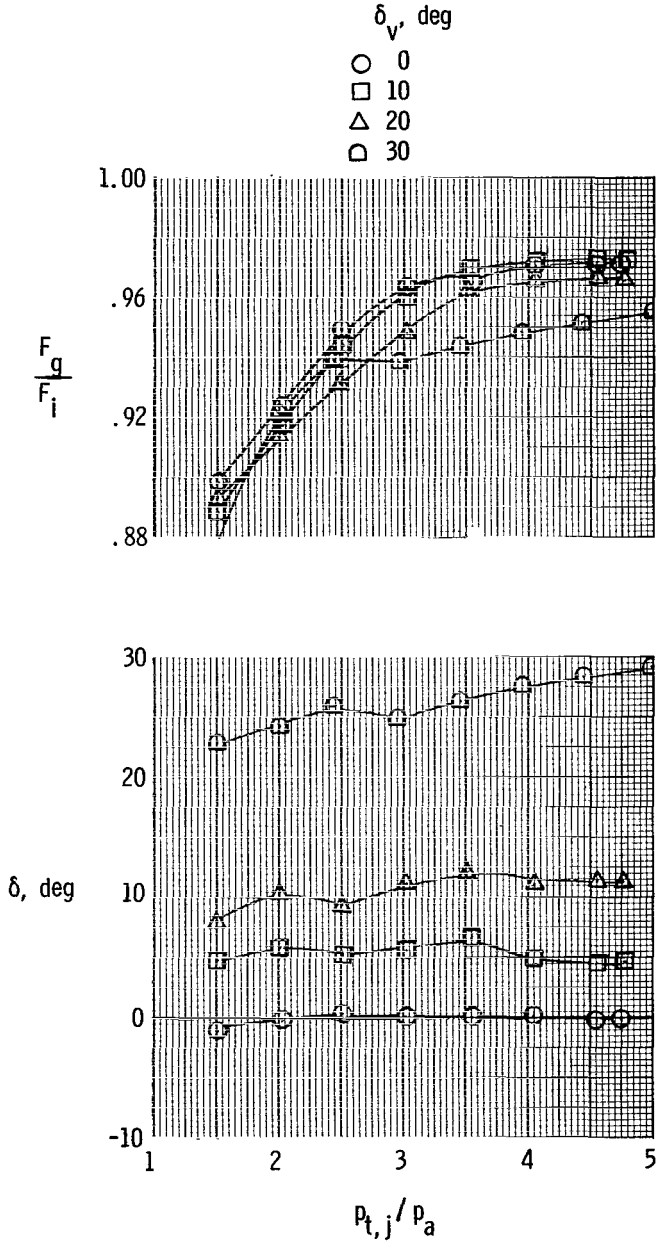

(b) Intermediate power.

Figure 17.- Continued.

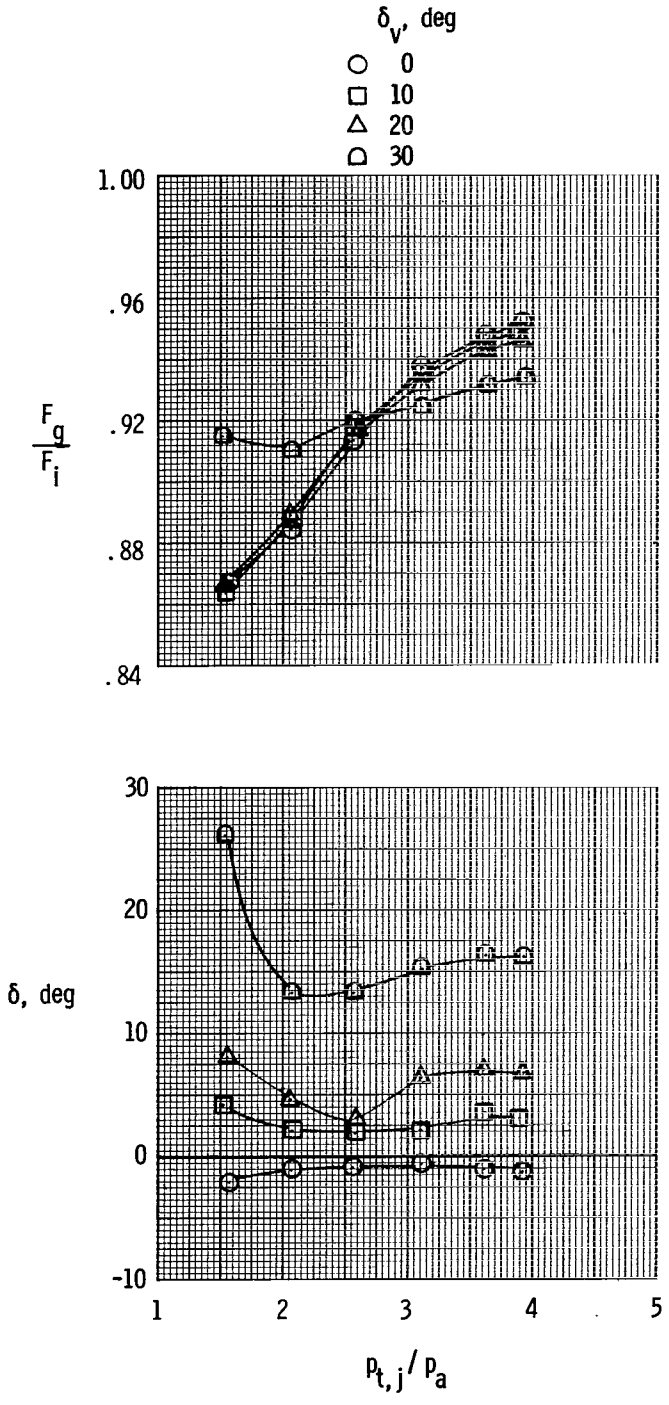

(c) Maximum power.

Figure 17.- Concluded.

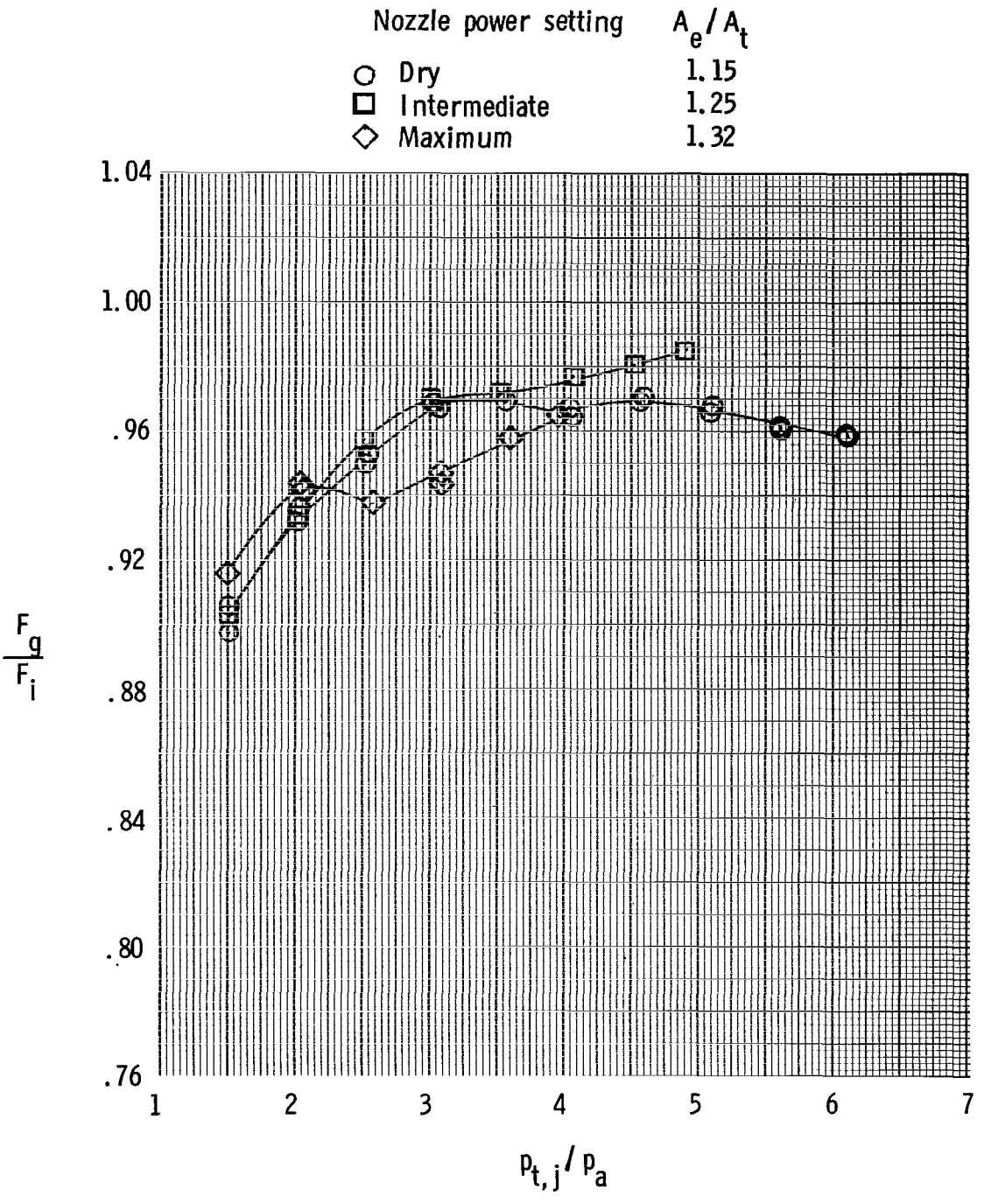

Figure 18.- Static performance characteristics of wedge nozzle 2.

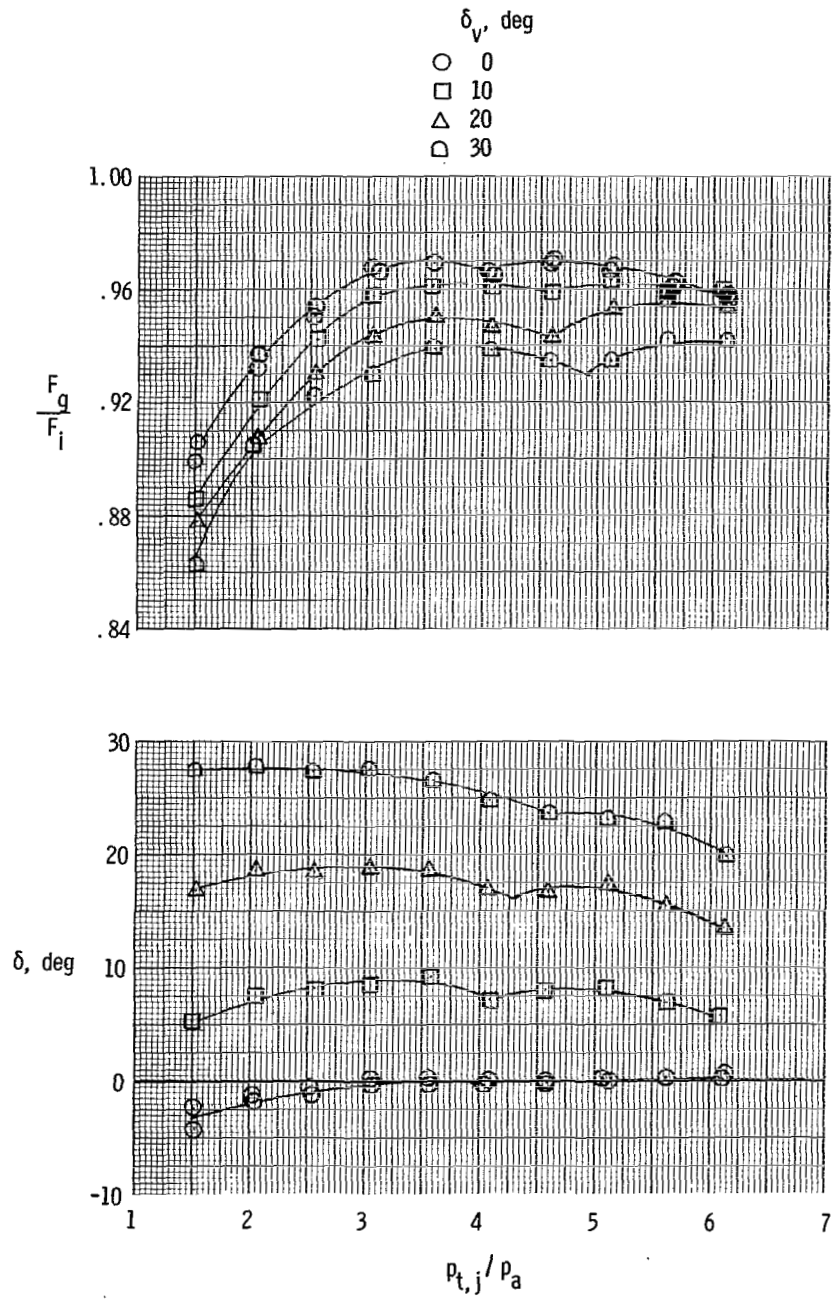

(a) Dry power.

Figure 19.- Static vectoring performance of wedge nozzle 2.

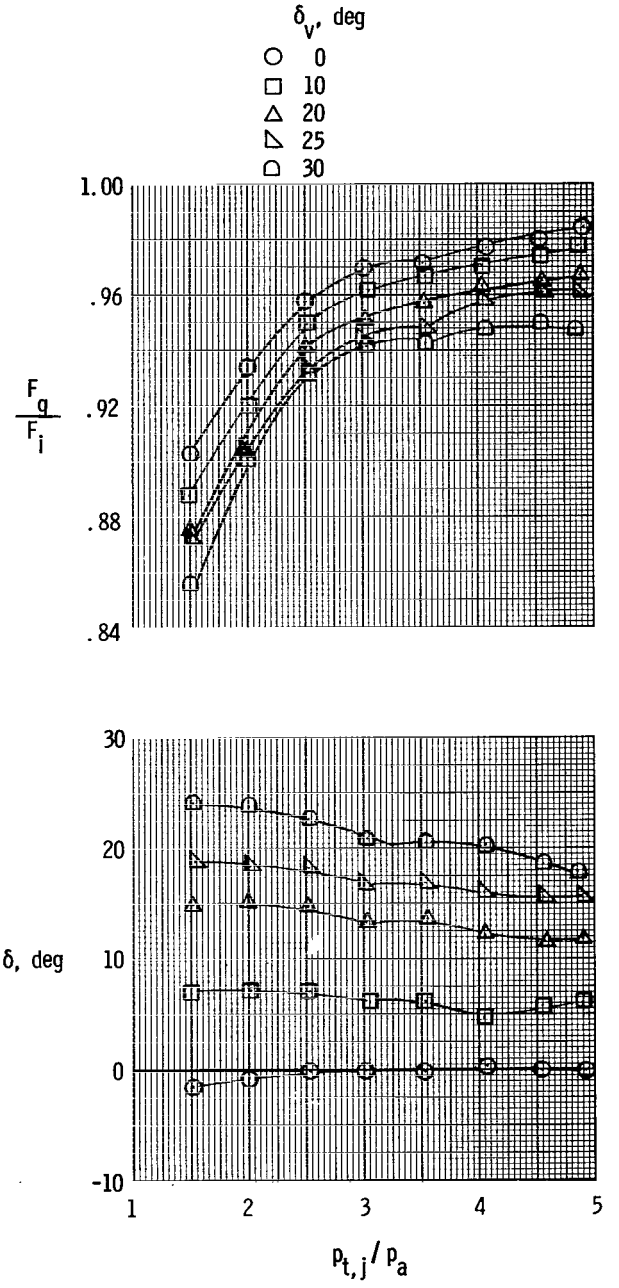

(b) Intermediate power.

Figure 19.- Continued.

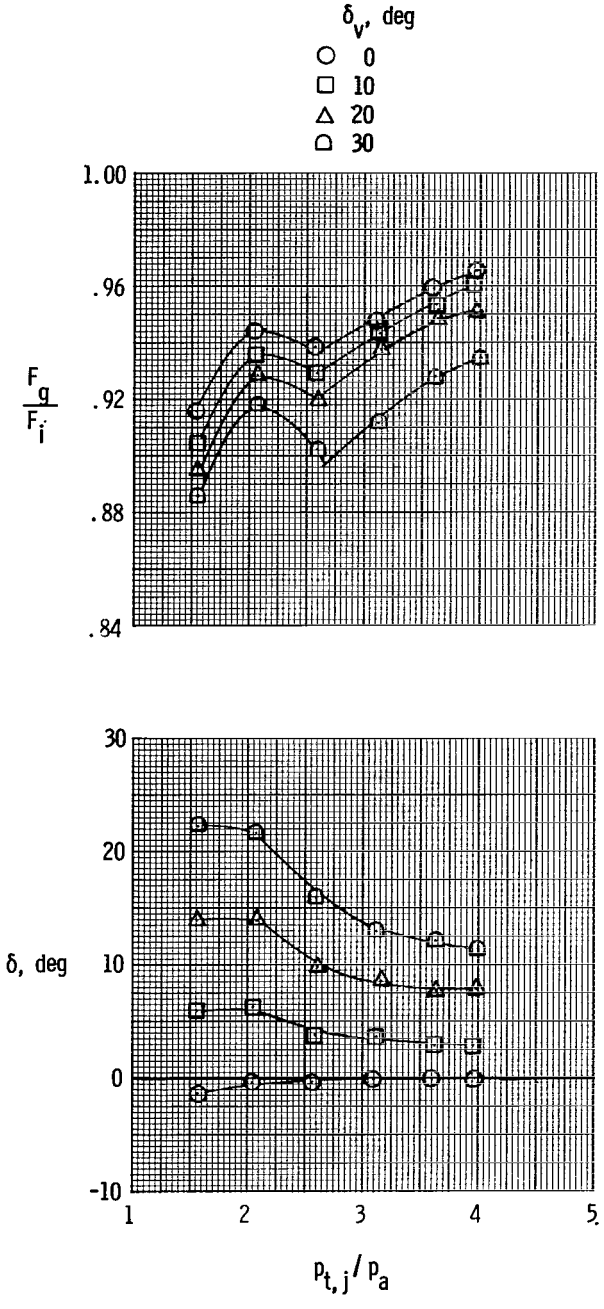

(c) Maximum power.

Figure 19.- Concluded.

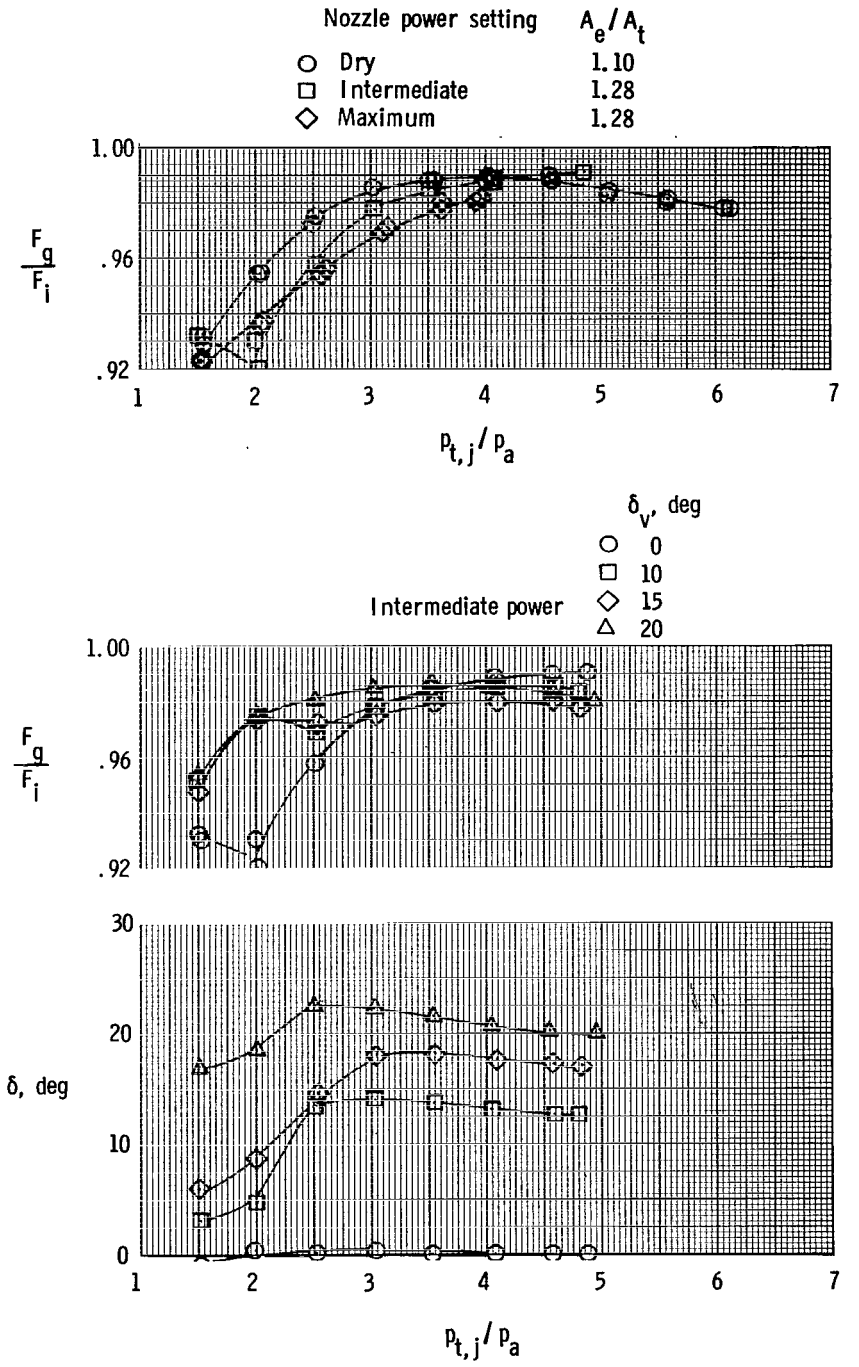

Figure 20.- Static performance and vectoring characteristics of the 2-D C-D/1 nozzle.

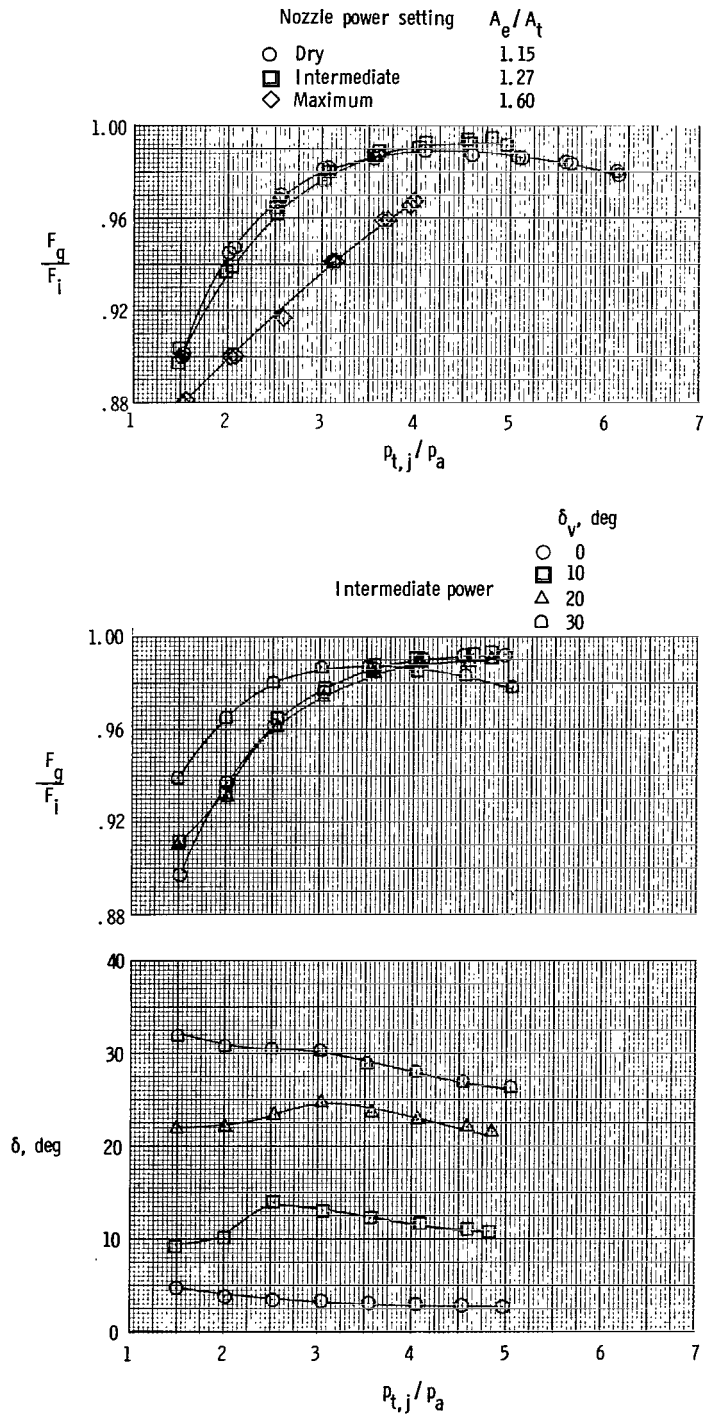

Figure 21.- Static performance and vectoring characteristics of the 2-D C-D/2 nozzle.

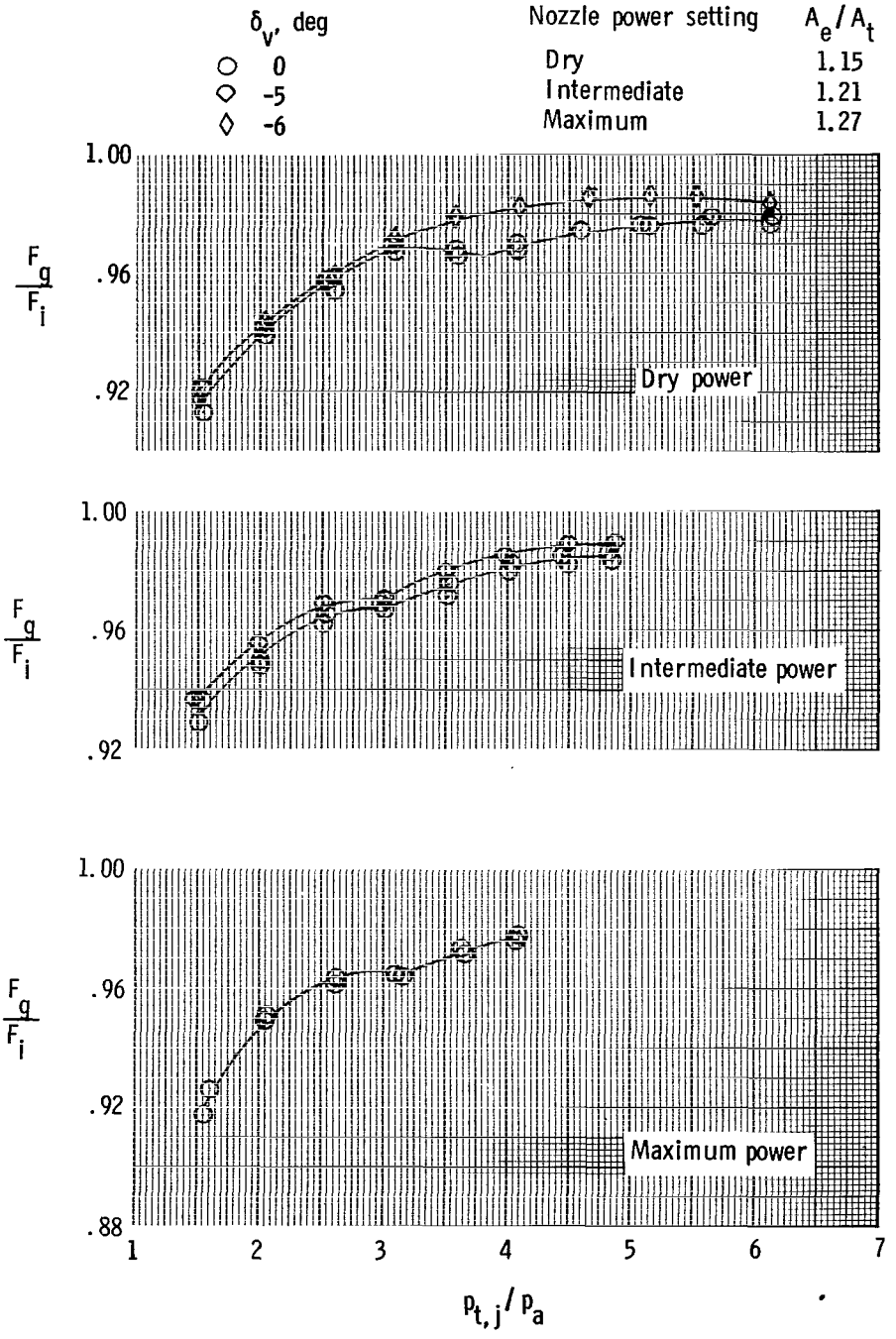

Figure 22.- Static performance characteristics of single-expansion ramp nozzle.

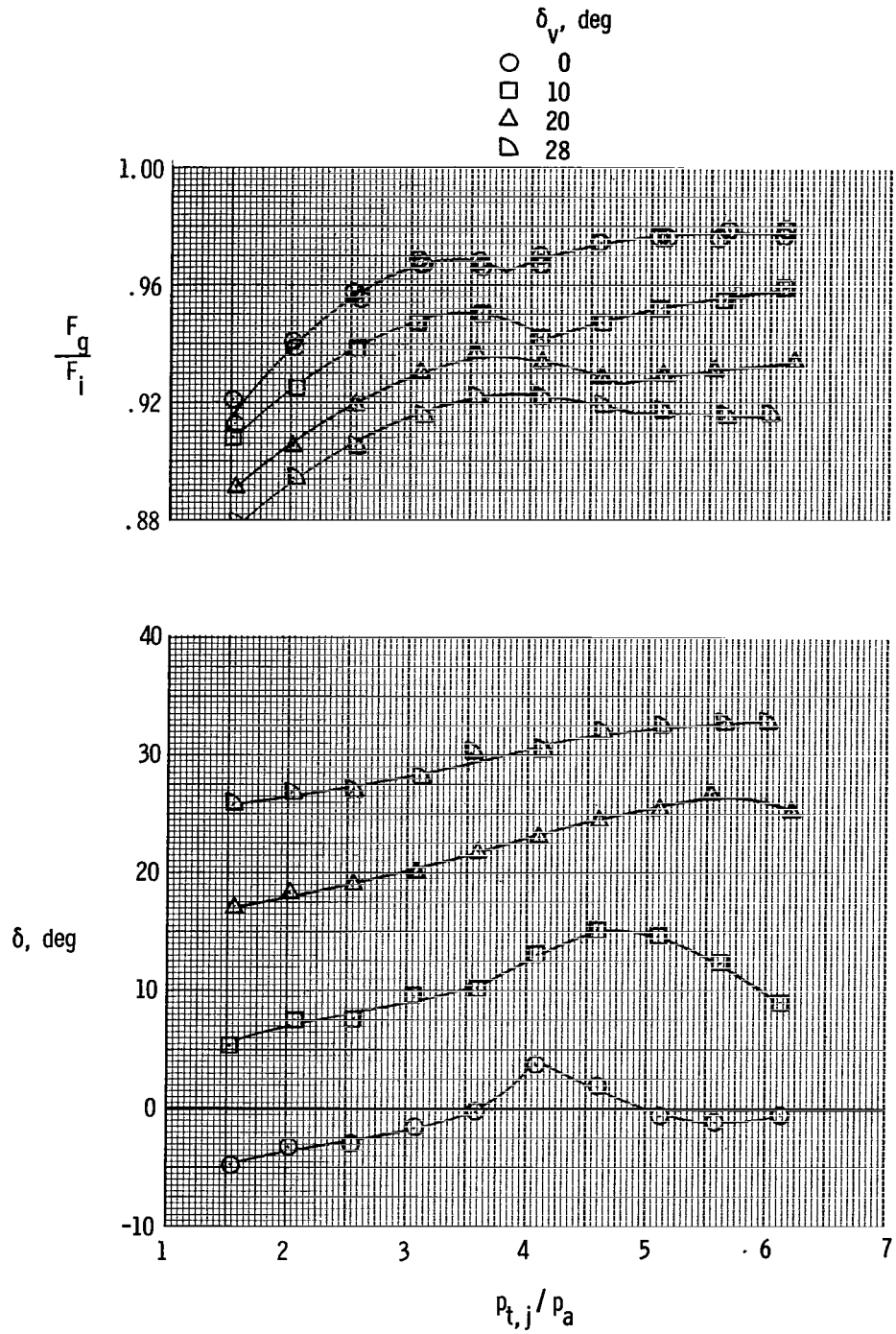

(a) Positive vectoring.

Figure 23.- Static vectoring performance characteristics of single-expansion ramp nozzle with dry power.

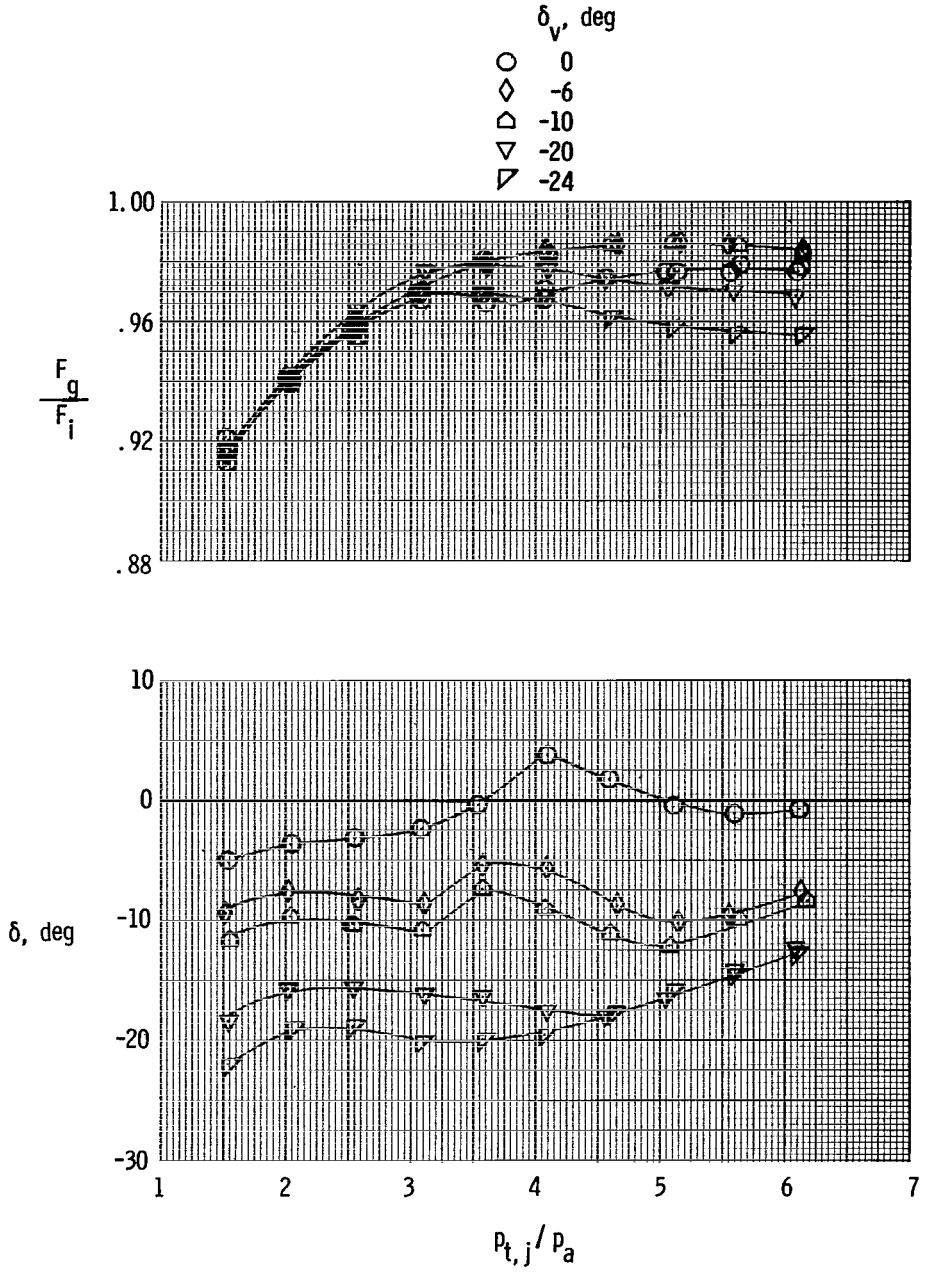

(b) Negative vectoring.

Figure 23.- Concluded.

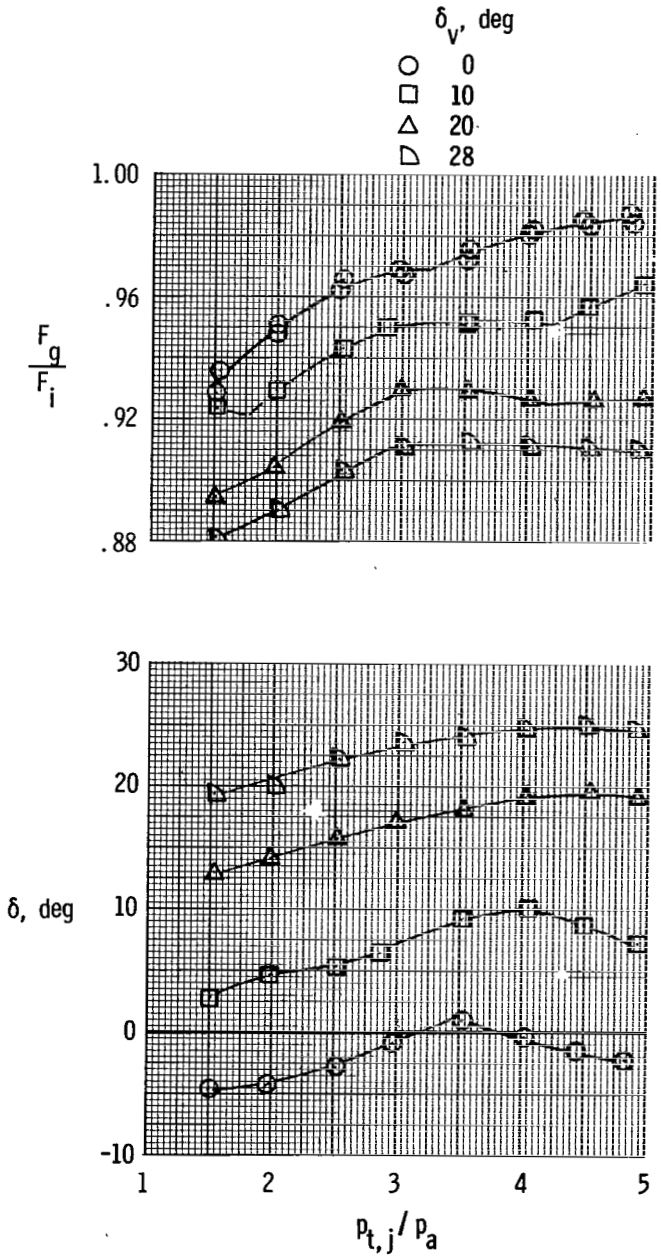

(a) Positive vectoring.

Figure 24.- Static vectoring performance characteristics of single-expansion ramp nozzle with intermediate power.

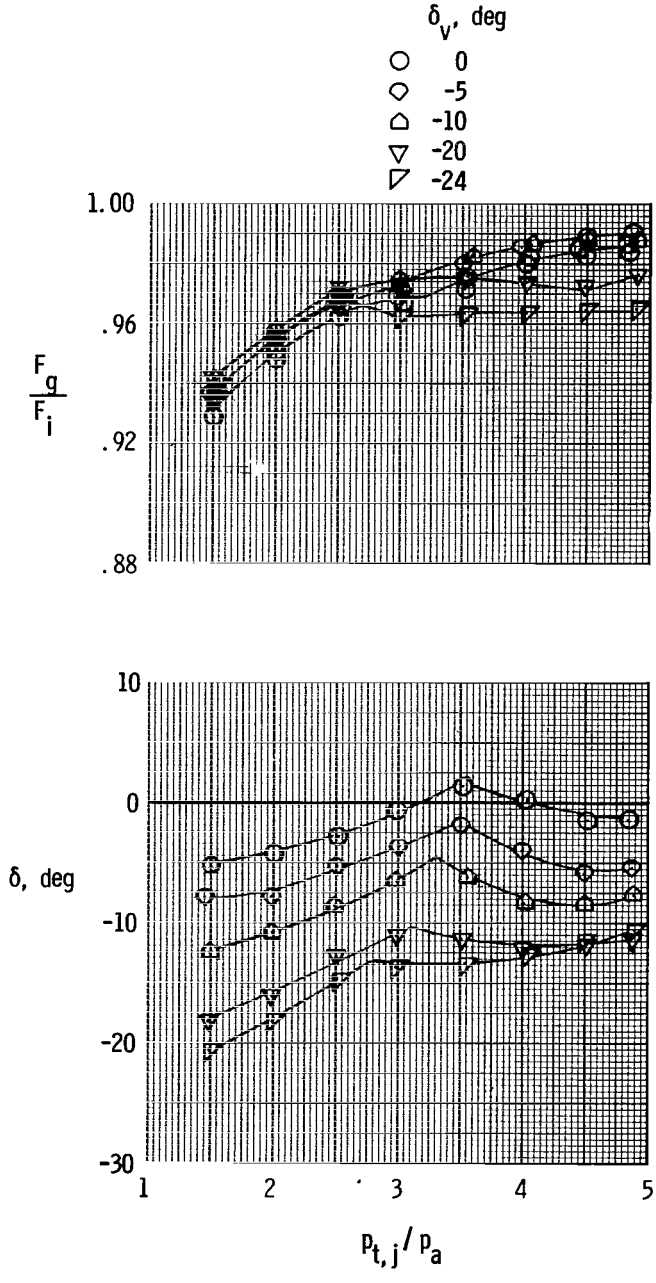

(b) Negative vectoring.

Figure 24.- Concluded.

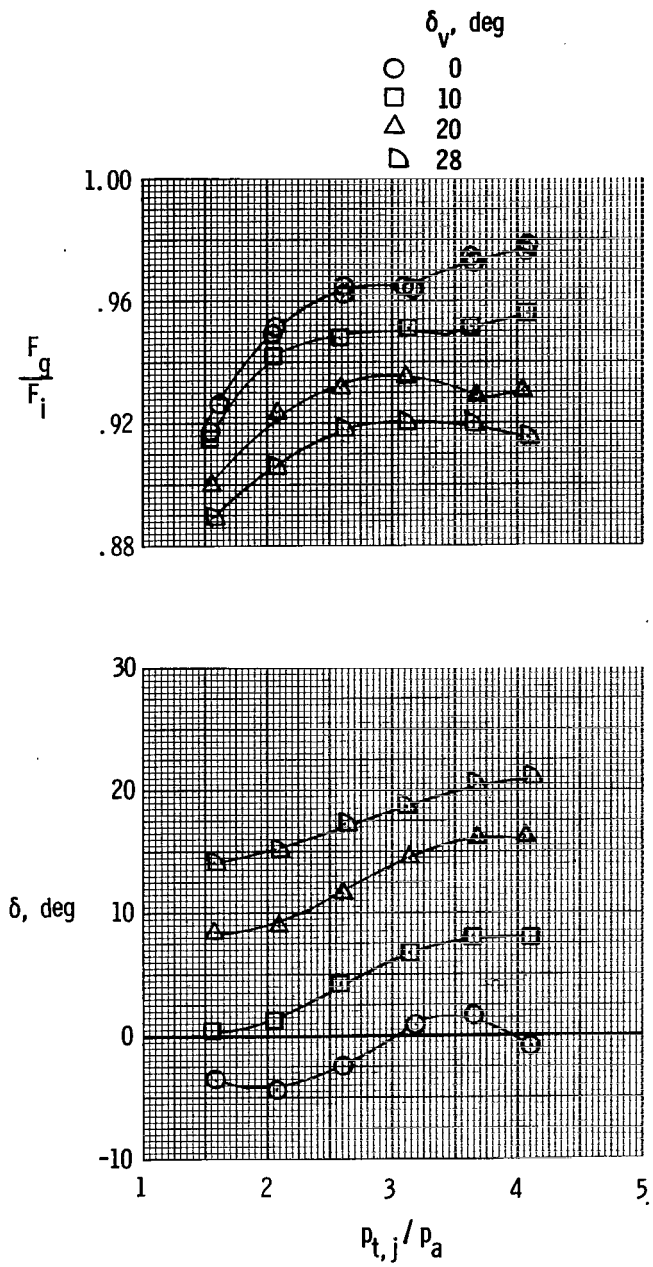

(a) Positive vectoring.

Figure 25.- Static vectoring performance characteristics of single-expansion ramp nozzle with maximum power.

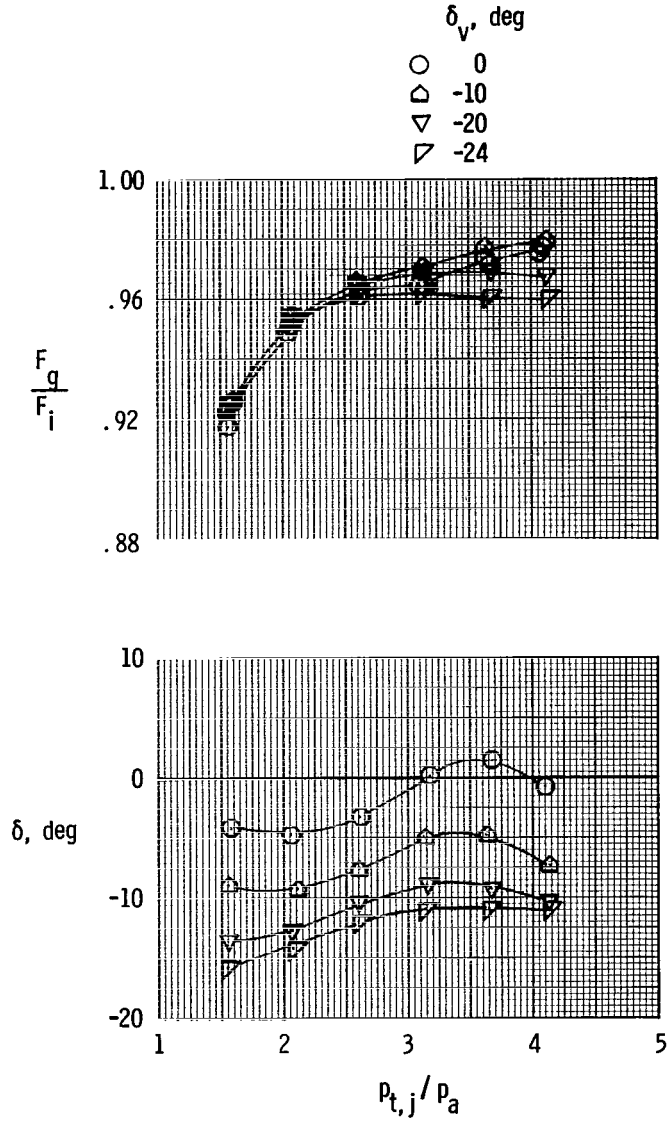

(b) Negative vectoring.

Figure 25.- Concluded.

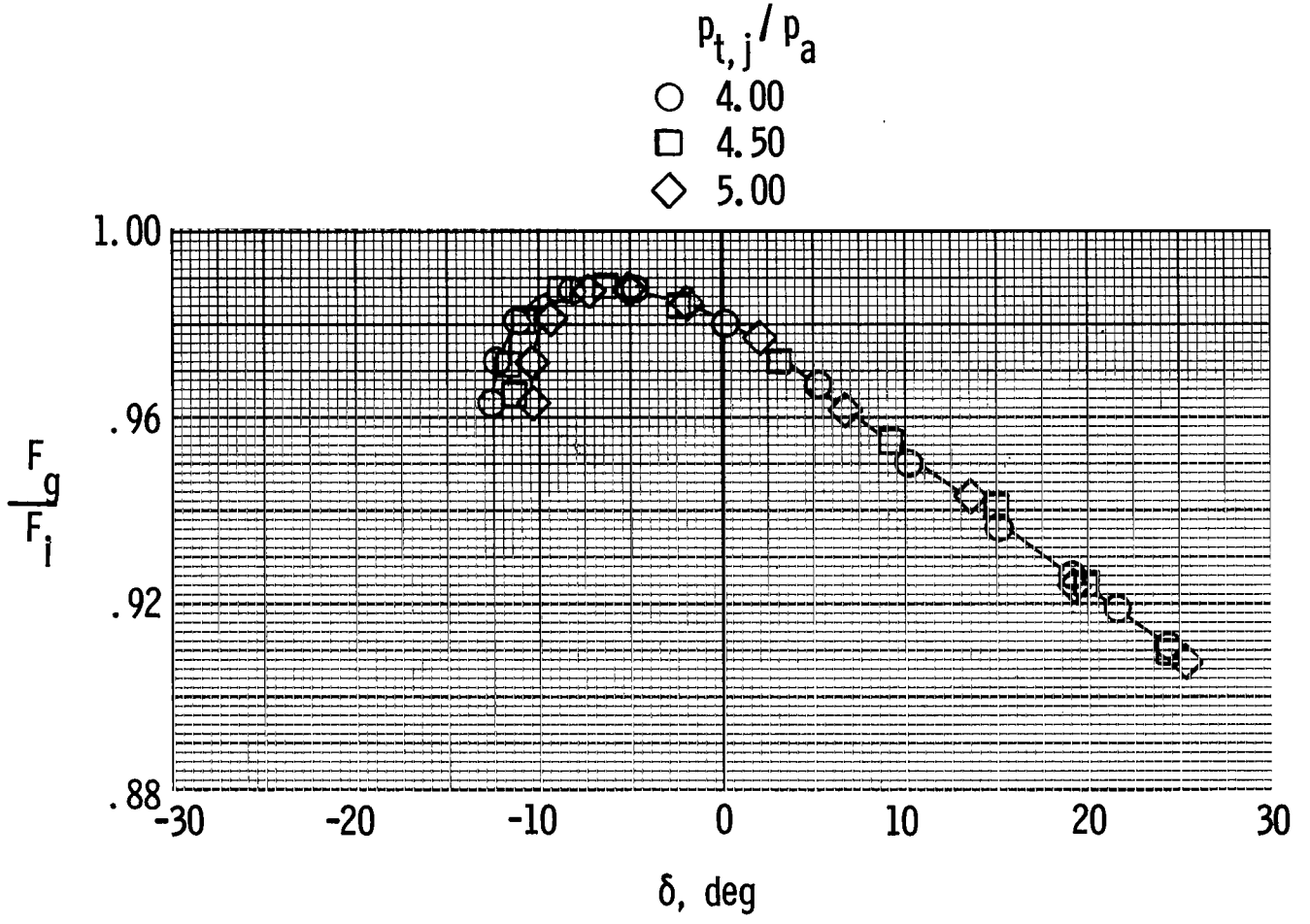

Figure 26.- Effect on static performance of varying vector angle at constant nozzle pressure ratio for single-expansion ramp nozzle with intermediate power.

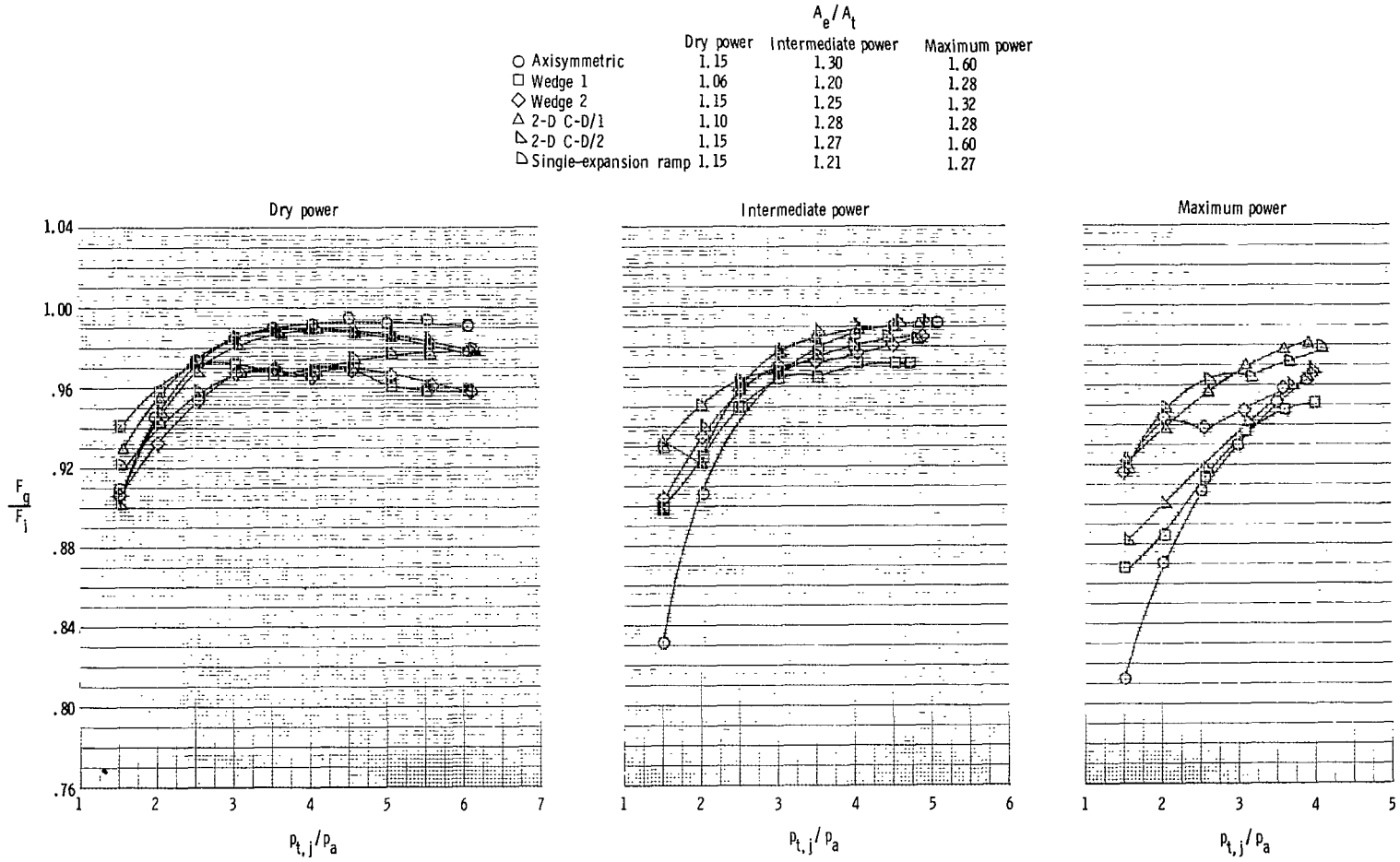

Figure 27.- Comparison of static performance of all nozzles tested. $\delta_v = 0^o$.

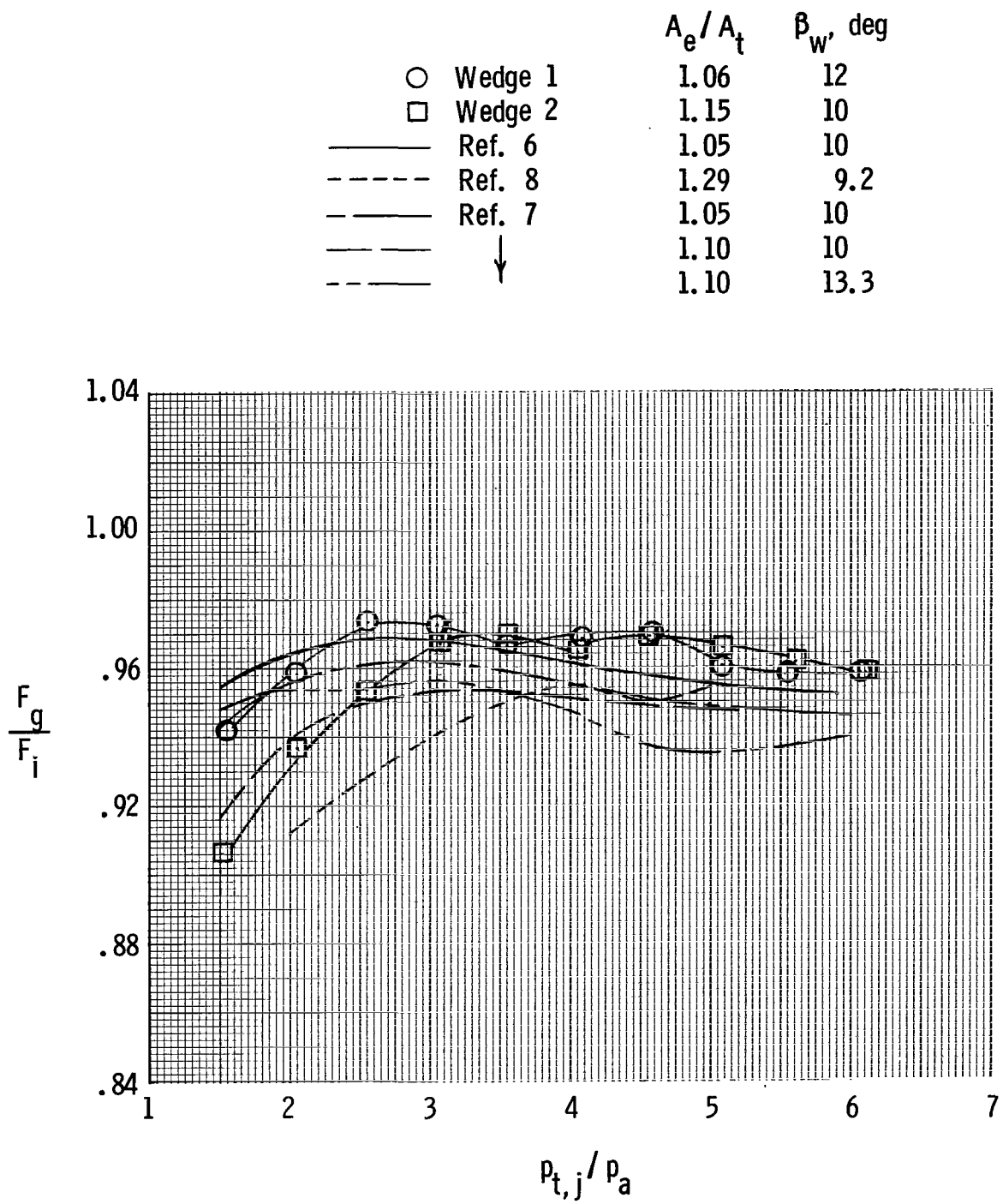

Figure 28.- Comparison of static performance of wedge nozzle from present investigation with other data. Dry-power nozzle settings only.

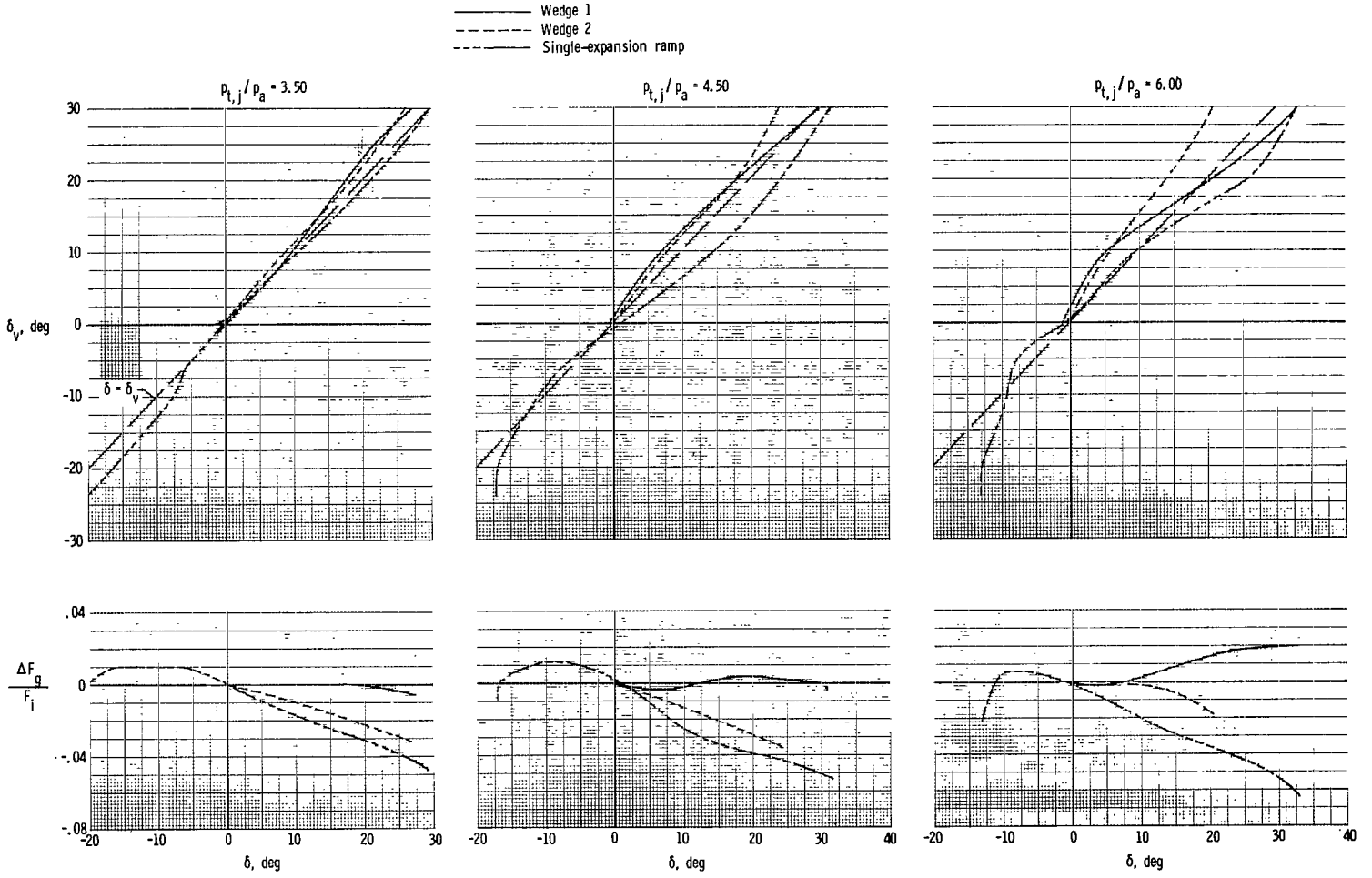

(a) Dry power.

Figure 29.- Summary of nozzle static turning and vectoring performance characteristics at constant pressure ratio.

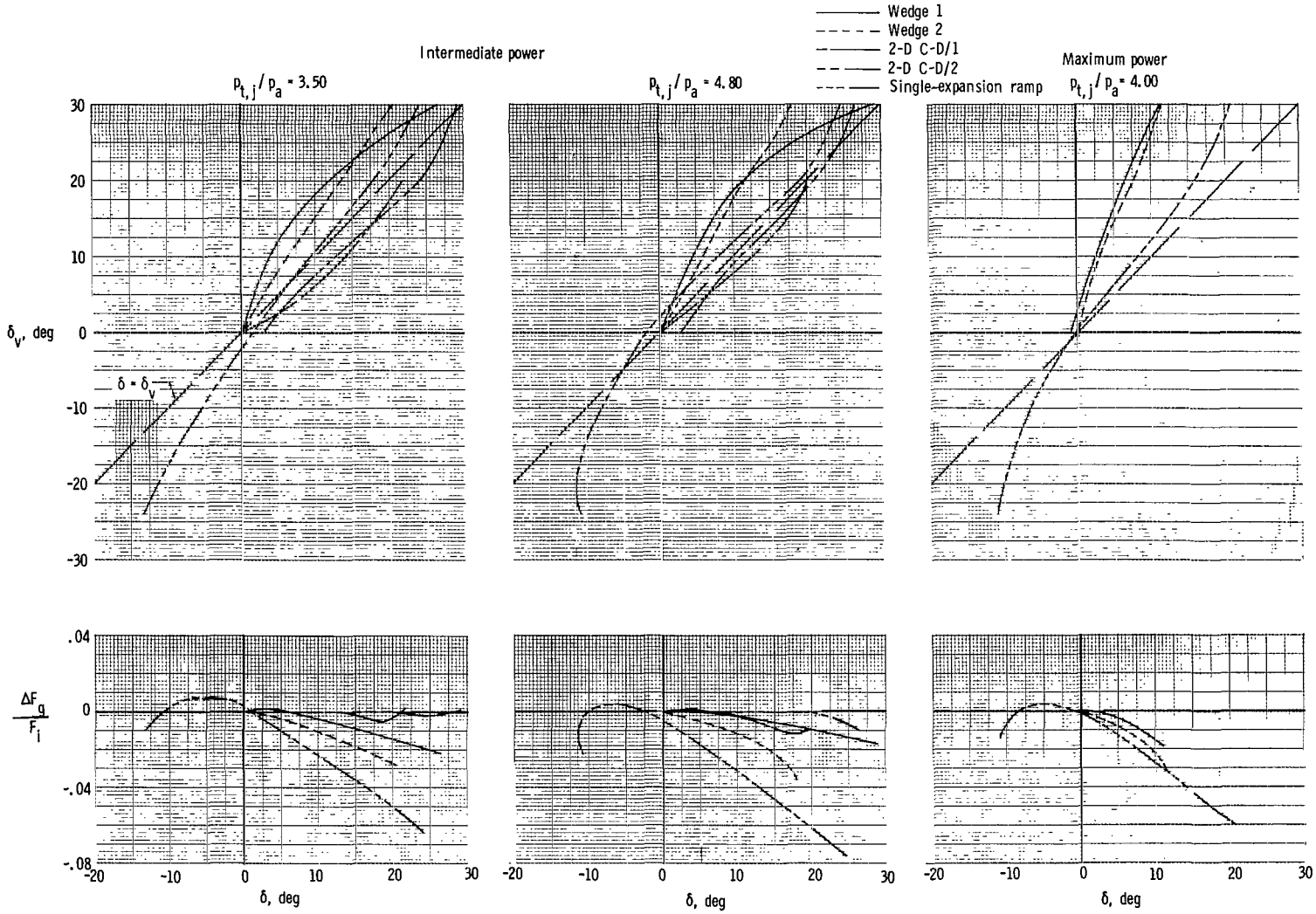

(b) Afterburner power.

Figure 29.- Concluded.

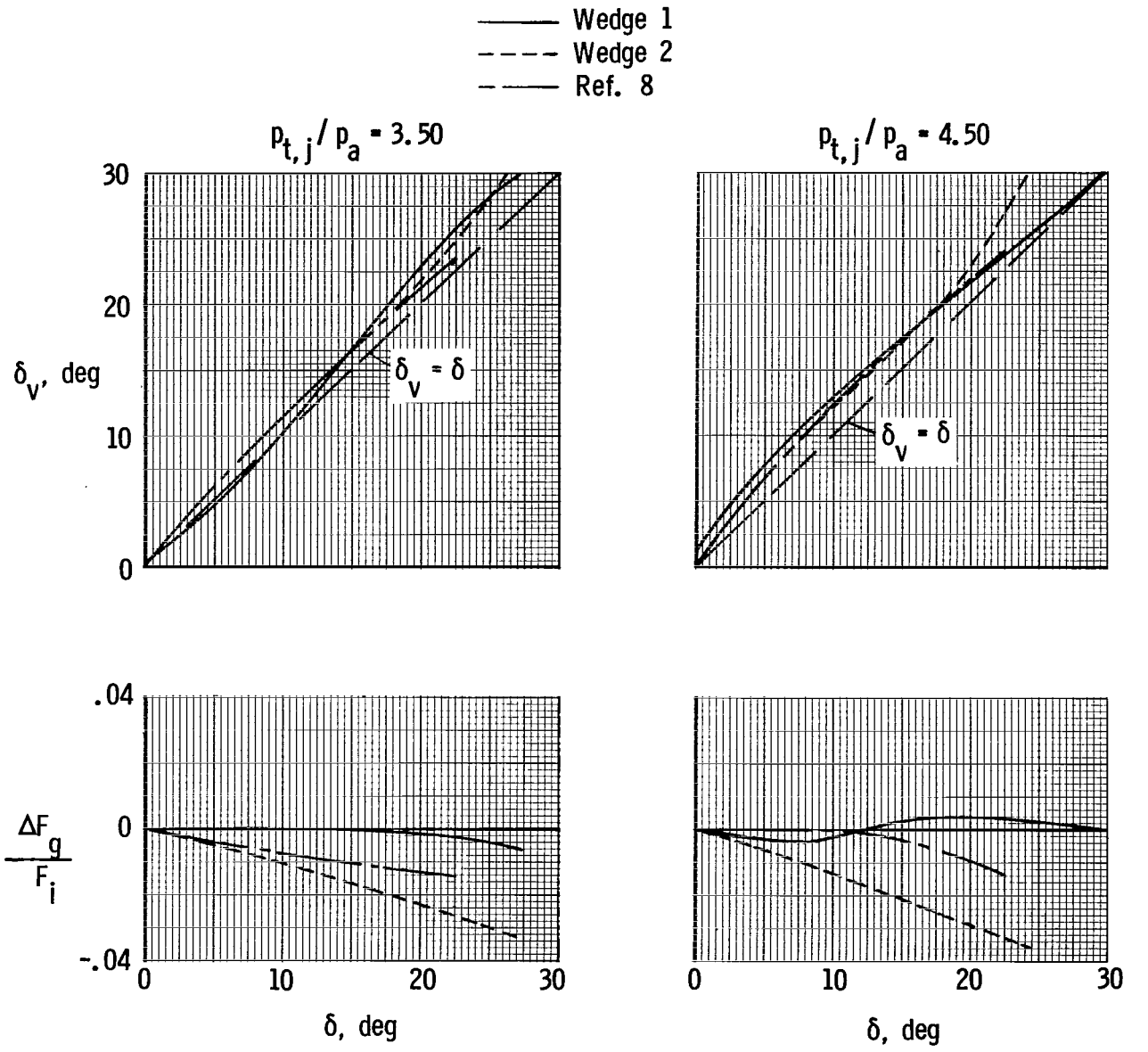

Figure 30.- Comparison of static vectoring performance of wedge nozzles of present investigation with other data with dry power.

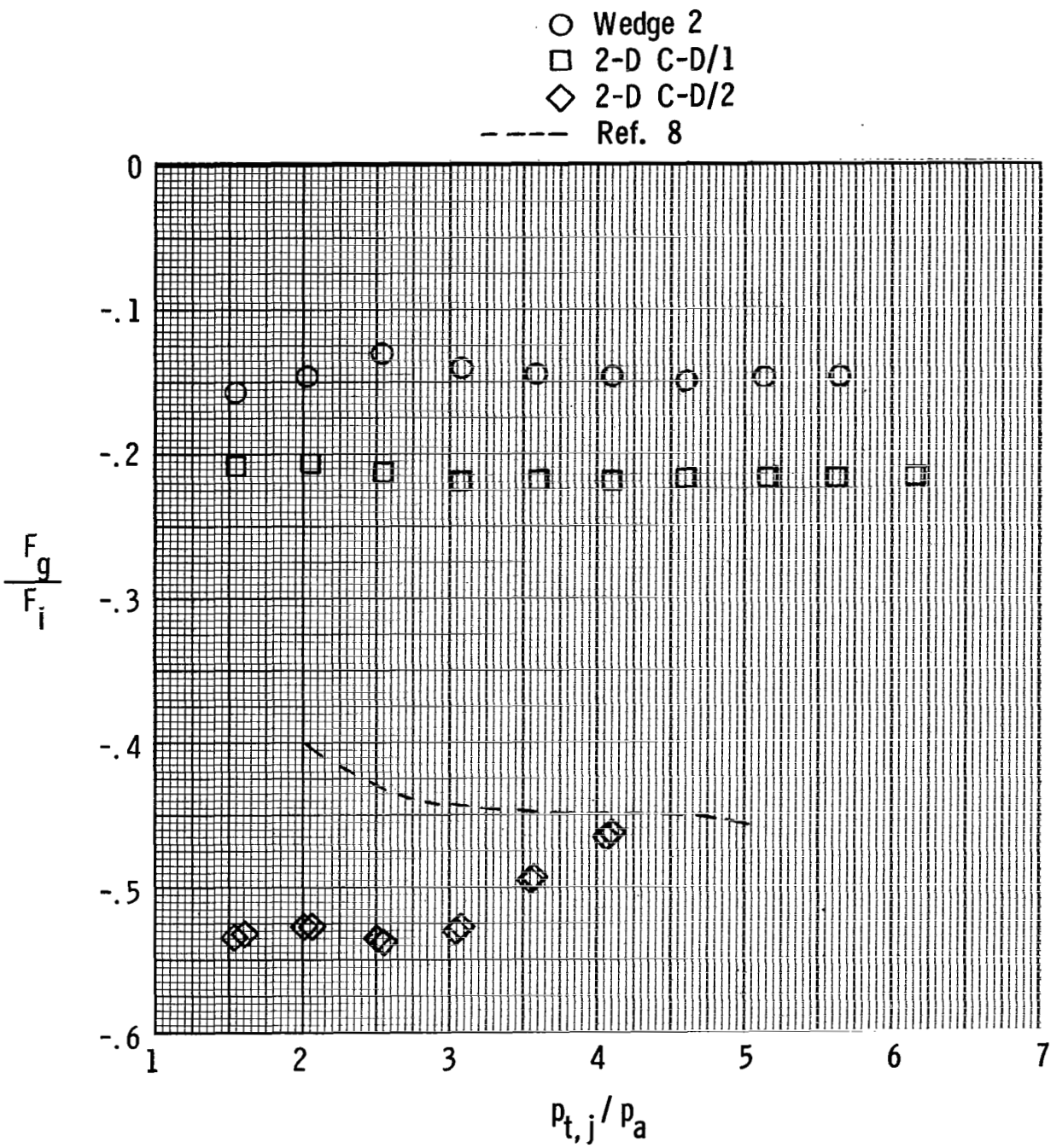

Figure 31.- Reverse thrust characteristics of three nozzles tested with dry power.

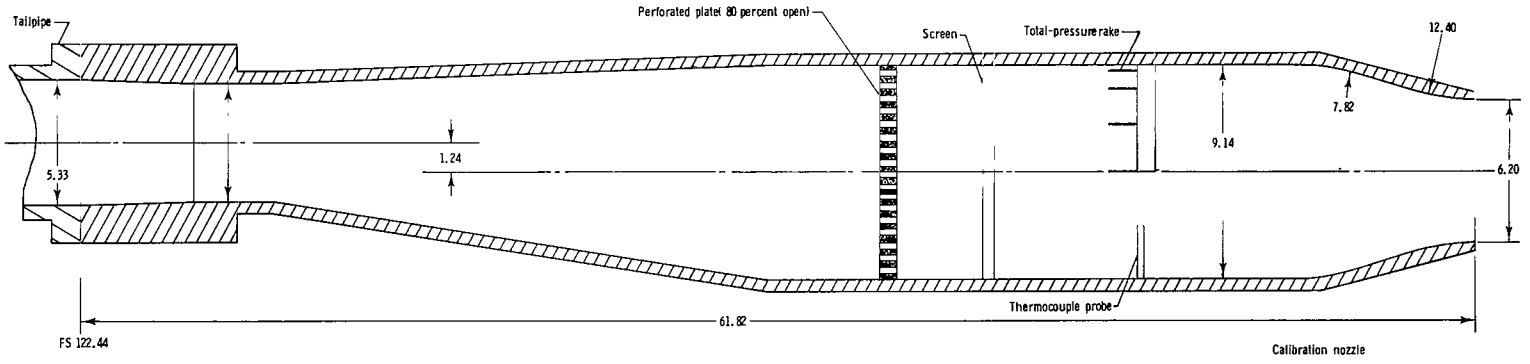

Power setting	d_t	X_t
Dry	4.63	9.95
Intermediate	6.21	8.14
Maximum	7.31	6.43

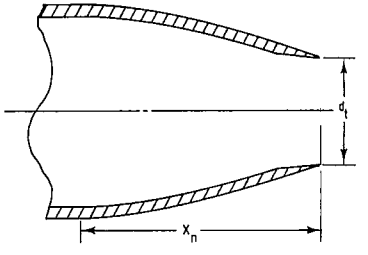

Figure 32.- Sketch of calibration and iris-convergent nozzles. All dimensions are in centimeters unless otherwise noted.

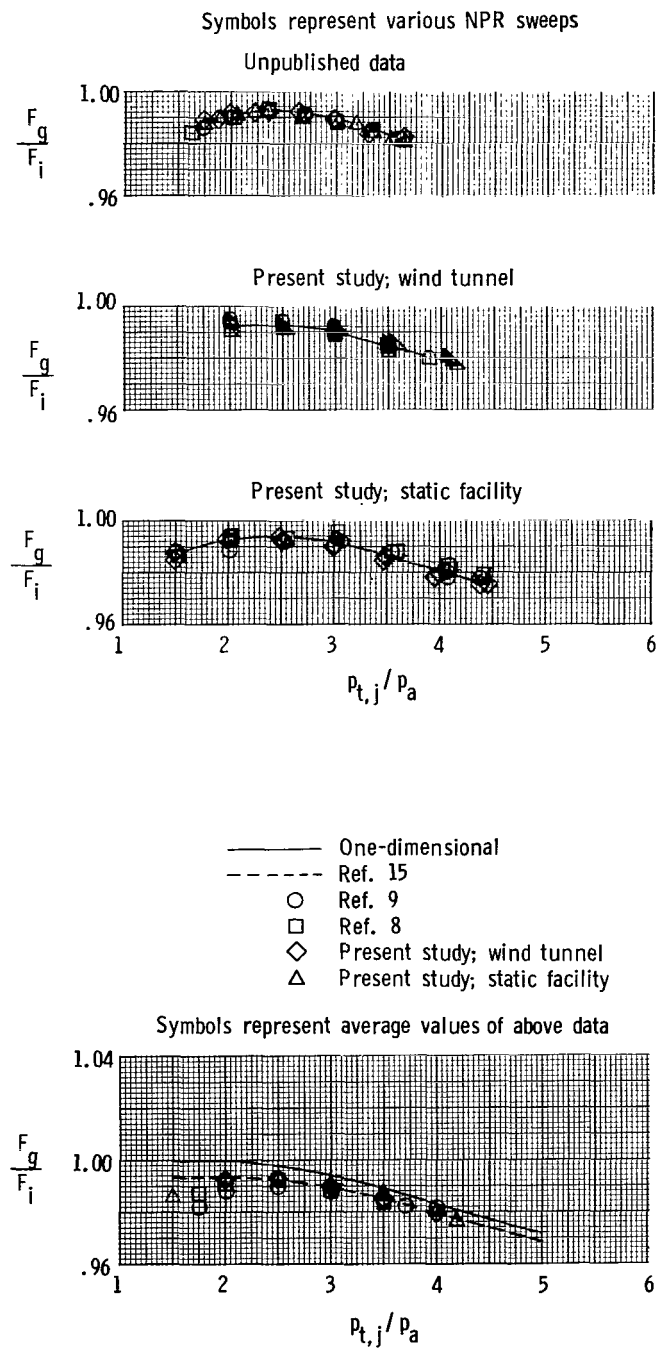

Figure 33.- Summary of performance characteristics of calibration nozzles. Discharge coefficient varies from 0.990 to 0.995 for all of above data.

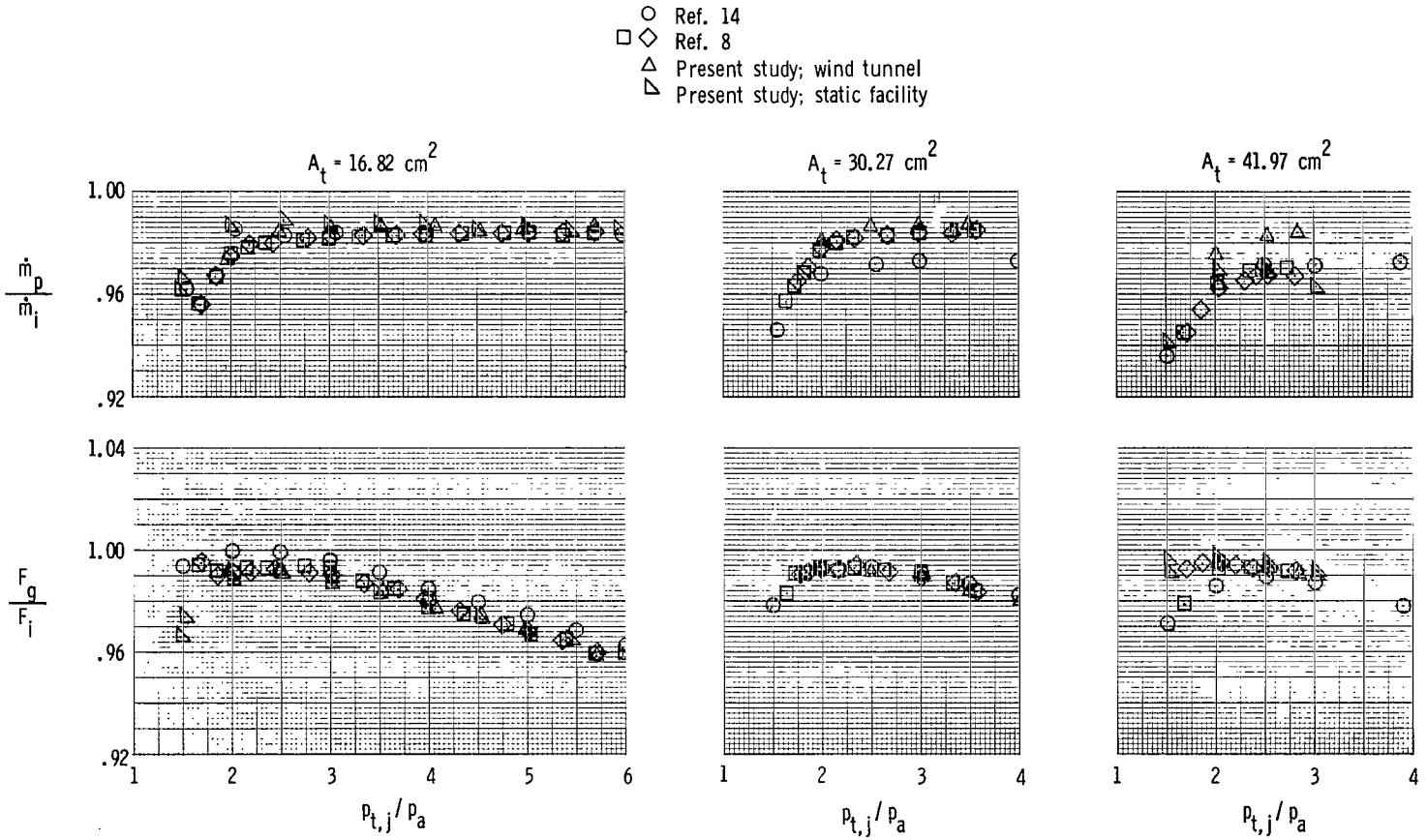

Figure 34.- Summary of performance characteristics of iris-convergent nozzles of reference 14. Symbols for reference 14 represent average values only for performance data.

1. Report No.	2. Government Accession No.	3. Recipient's Catalog No.
NASA TP-1224		

4. Title and Subtitle	5. Report Date
STATIC PERFORMANCE OF FIVE TWIN-ENGINE NONAXISYMMETRIC NOZZLES WITH VECTORING AND REVERSING CAPABILITY	July 1978
	6. Performing Organization Code
7. Author(s)	8. Performing Organization Report No.
Francis J. Capone	L-12067
	10. Work Unit No.
9. Performing Organization Name and Address	505-11-23-06
NASA Langley Research Center Hampton, VA 23665	11. Contract or Grant No.
	13. Type of Report and Period Covered
12. Sponsoring Agency Name and Address	Technical Paper
National Aeronautics and Space Administration Washington, DC 20546	14. Sponsoring Agency Code

15. Supplementary Notes

16. Abstract

An investigation has been conducted in the static-test facility of the Langley 16-foot transonic tunnel to determine the static performance of five twin-engine nonaxisymmetric nozzles and a base-line axisymmetric nozzle at three nozzle power settings. Static thrust-vectoring and thrust-reversing performance were also determined. Nonaxisymmetric-nozzle concepts included two-dimensional convergent-divergent nozzles, wedge nozzles, and a nozzle with a single external-expansion ramp. All nonaxisymmetric nozzles had essentially the same static performance as the axisymmetric nozzle. Effective thrust vectoring and reversing was also achieved.

17. Key Words (Suggested by Author(s))	18. Distribution Statement
Axisymmetric nozzles Nonaxisymmetric nozzles Thrust-vectoring nozzles Thrust-reversing nozzles	Unclassified - Unlimited Subject Category 02

19. Security Classif. (of this report)	20. Security Classif. (of this page)	21. No. of Pages	22. Price*
Unclassified	Unclassified	63	$5.25

* For sale by the National Technical Information Service, Springfield, Virginia 22161

NASA-Langley, 1978

National Aeronautics and
Space Administration

Washington, D.C.
20546

Official Business
Penalty for Private Use, $300

THIRD-CLASS BULK RATE

Postage and Fees Paid
National Aeronautics and
Space Administration
NASA-451

U.S.MAIL

2 1 1U,A, 072178 S00903DS
DEPT OF THE AIR FORCE
AF WEAPONS LABORATORY
ATTN: TECHNICAL LIBRARY (SUL)
KIRTLAND AFB NM 87117

NASA

POSTMASTER: If Undeliverable (Section 158 Postal Manual) Do Not Return